Summer 2018

Fabrication of an Apparatus for All-Optical Production of Metastable Krypton

Lindsay M. Thornton
Old Dominion University

FABRICATION OF AN APPARATUS FOR ALL-OPTICAL PRODUCTION OF METASTABLE KRYPTON

by

Lindsay M. Thornton
B.A. May 2003, Washington College
B.S. May 2016, East Carolina University

A Thesis Submitted to the Faculty of
Old Dominion University in Partial Fulfillment of the
Requirements for the Degree of

MASTER OF SCIENCE

PHYSICS

OLD DOMINION UNIVERSITY
August 2018

Approved by:

Charles Sukenik (Director)

Gail Dodge (Member)

Alexander Gurevich (Member)

ABSTRACT

FABRICATION OF AN APPARATUS FOR ALL-OPTICAL PRODUCTION OF METASTABLE KRYPTON

Lindsay M. Thornton
Old Dominion University, 2018
Director: Dr. Charles Sukenik

Atom Trap Trace Analysis (ATTA) has made radiokrypton dating of polar ice and groundwater samples a possibility for scientists all over the world, allowing them to date samples further back in time and more accurately than other methods. However, this technique is hampered by the 36-hour cleaning process required for production of metastable-state krypton atoms via a radio-frequency driven plasma. Production of metastable krypton all-optically would dramatically increase the rate at which samples could be measured. Attempts to build an apparatus that could accomplish this have been done in the past but were lacking in affordability and practicality for widespread use. Using a newly available, commercial 123nm lamp, as well as an 819nm external cavity diode laser combined with a Fabry-Perot power buildup cavity may solve both of those problems. The work reported here details progress made on our experiment to investigate all-optical production of metastable-state krypton. While our apparatus is expected to be both affordable and portable, it still requires optimization in a variety of areas including stabilization of the Fabry-Perot cavity, final choice of the best cavity configuration that optimizes high intensity vs. large beam waist and, finally, detection optimization. With further study, this experiment will allow us to quantify the rate of metastable state krypton produced in this new excitation configuration and inform final design of a module to produce metastable krypton that has the potential to be an improvement for ATTA by increasing the rate at which samples can be dated for scientists around the world.

ACKNOWLEDGEMENTS

I would like to thank my thesis advisor, Dr. Charles Sukenik, of the Physics Department at Old Dominion University, the Yoda of Experimental Optics. He took me under his wing and shared his knowledge and enthusiasm for experimental physics. He was infinitely patient and always supportive. This was a priceless opportunity and it has taught me so much. I would also like to thank Grady White, PhD graduate student in the Physics Department at Old Dominion University. I am indebted to him for all his help, insight, and support. He allowed me to pester him like a big brother and anytime I needed gas he was there to assist. I would like to acknowledge the contributions of Hauke Busch, Will Williams, Z.-T. Lu and Argonne National Lab to this project. I would like to acknowledge Dr. Alexander Gurevich and Dean Gail Dodge as committee members for this thesis. I am gratefully indebted to them for very valuable comments on this thesis and for sitting on my committee. I would also like to acknowledge Lisa Okun, whose tireless efforts to support the Old Dominion graduate students does not go unnoticed by the students! She is, perhaps, the most valuable member of the department. I would like to thank Josh Frechem and Simon Maddock for their invaluable assistance in the lab. They were intelligent and insightful, as well as good company. And, of course, I would not be here without my friends Jeremy Peshl, Josh Yoskowitz, and Tyler Viducic. Whether helping me talk things out, working on fixing latex issues, or convincing me to take a break, they made being here a lot more fun. Finally, I must express my very profound gratitude to my parents and to my boyfriend, Logan, for providing me with unfailing support and continuous encouragement throughout my years of study and through the process of researching and writing this thesis. (Thank you for putting up with me.)

Lindsay

Thornton

TABLE OF CONTENTS

Page

LIST OF TABLES

LIST OF FIGURES

CHAPTER 1

INTRODUCTION

For more than 70 years, scientists in geology, hydrology, geophysics, atmospheric science, oceanography, paleoclimatology and even bio-medicine, have relied upon radiocarbon dating to revolutionize humankind's understanding of our past, as well as the present. However, as science moves forward so does the ever-present need to increase man's ability to probe the past of not only human history, but the history of our entire planet. In our need to look back further and further into earth's past we require new techniques and tools to do so, including using a greater number of radioisotopes to cover an ever-widening range of dating applications.

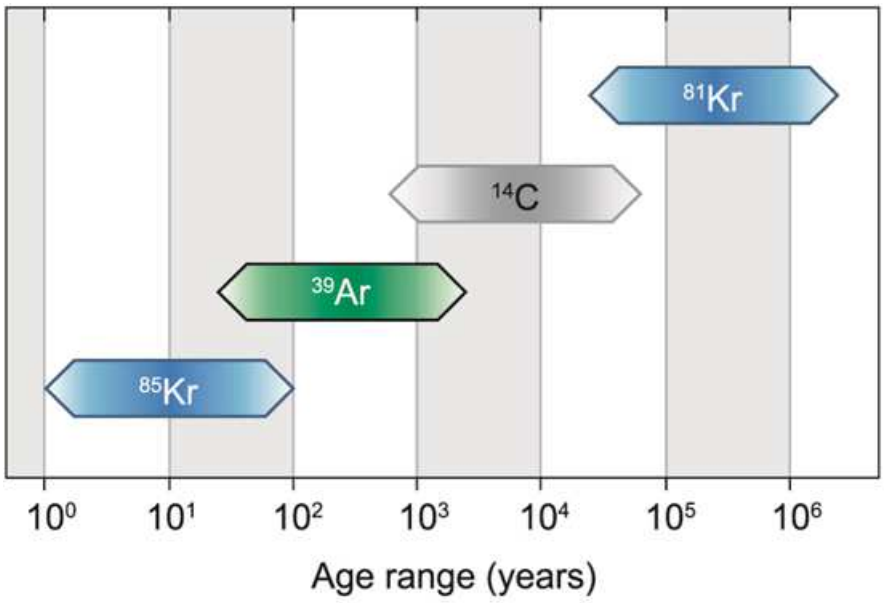

FIG. 1: The applicable age ranges of radio-isotope dating using ^{85}Kr, ^{39}Ar, ^{14}C, and ^{81}Kr. (Figure credit: Peter Mueller) [1].

FIG. 1 shows the dating ranges of ^{85}Kr, ^{39}Ar, ^{81}Kr and other established radioisotope tracers and the age ranges over which they are considered reliable [1]. Notice that carbon-14 on its own can only cover a limited age range, however, using krypton

and argon isotopes increases the reliably dateable age range from the present, all the way back to approximately 1.5 million years ago. Krypton-81 has been recognized as a desirable dating tool for old groundwater and polar ice because it can date so far back in time, coinciding with the suspected age of some of the oldest ice on earth [2].

1.1 BACKGROUND

While expanding the use of a variety of noble gases for radioisotope dating is desirable for a variety of applications, measurement techniques for radioisotope tracers must be able to meet the necessary demand of resolution down to the single atom regime to be useful for current dating techniques. The newest method in routine use, Atom Trap Trace Analysis (ATTA), is a laser based counting method free of interference from other isotopes, isobars and molecular species, making it unique among the trace analysis techniques [3]. This apparatus cools, slows, and captures the atoms using a 3D magneto-optical trap loaded by a Zeeman-slower.

The metastable Kr atoms are transverse-cooled first in order to reduce the divergence of the atomic beam and amplify the atom flux, and then they are slowed by a Zeeman Slower, an apparatus of magnetic coils that tunes the atoms, keeping them continually on resonance with the counter propagating laser that slows (cools) the atoms in one dimension, in preparation for the magneto-optical trap (MOT)[4].

The MOT can then further cool and trap these atoms. The MOT uses a pair of magnetic field coils in anti-Helmholtz configuration to create a quadrupole field that goes to zero at the center. Combined with three pairs of counter-propagating laser beams, detuned below resonance, and with opposite circular polarization, the laser beams cool and confine the atoms. The Doppler shift of the atoms gives rise to a velocity dependent force (cooling) and the non-uniform magnetic field gives rise to a spatially-dependent force (trapping). Atoms that enter the MOT region below a certain velocity are rapidly cooled and trapped near the center.

In order to cool and trap the krypton atoms, they first need to be excited to a metastable state because the transition from the ground state to the first excited state is in the ultra-violet spectral region and no laser is available at that wavelength. The current apparatus for ATTA-3 uses a radio-frequency driven plasma to excite the krypton with a probability of 10^{-4} to the needed metastable state [5]. The measurement itself takes under 2 hours, but the apparatus must be cleaned for 36

hours before each measurement is taken. This is to be sure any krypton ionized during the excitation that may have embedded itself into the chamber walls is removed, lest it contaminate the next sample. This constraint affects the number of samples processed per year; the current laboratories that routinely krypton-date can only measure approximately 150-200 samples per year.

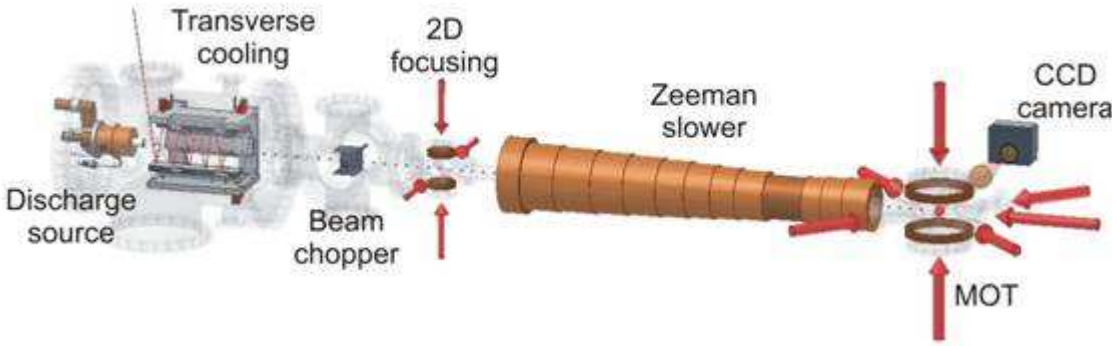

FIG. 2: Schematic of the ATTA-3 apparatus developed at Argonne National Laboratory [6].

The goal of this project is to design an affordable, reproducible apparatus that can replace the current RF plasma and instead all-optically produce the necessary metastables for use with ATTA, increasing the number of samples that each lab can measure per year.

1.2 HISTORY OF ALL-OPTICAL PRODUCTION

While other experiments have been performed to successfully produce metastable krypton none of them produced an apparatus that was easily reproduced, portable, and affordable. The first attempt, in 2002, L. Young et al. [7] used a home-built UV lamp to produce Kr atoms in the $5s[3/2]_{J=1}$ level, followed by using a Ti:sapphire laser to pump the atoms from $5s[3/2]_{J=1}$ to $5p[3/2]_{J=2}$. According to the authors, 77% of the atoms decayed to the metastable state however Ti:sapphire lasers are very expensive, costing upwards of $100,000, making this impractical for wide-spread usage. Also, the UV lamp was not commercially available and had problems with self-reversal and contamination of the magnesium fluoride window.

In 2014 a group from Hamburg, Germany, M. Kohler, et al. [8] produced metastable krypton all-optically using an array of eight home-built VUV lamps at 123.6 nm, each with an optical power <1mW that excited from the ground-level $4p^6\ {}^1S_{J=0}$ to the $5s[3/2]_{J=1}$ followed by the second excitation from $5s[3/2]_{J=1}$ to $5p[3/2]_{J=2}$ using a 1.4W 819 nm laser. While successful, with 75% of the excited atoms decaying to the metastable state, the number of lamps and the fact that they were not available commercially made this design impractical for widespread, inexpensive adoption.

In 2018 a group in Australia, with the University of Adelaide and Griffith University, explored the prospects of a laser-based two-photon excitation at 215nm (see FIG. 3). The 215nm light would excite the atoms into the short-lived $2p^6$ state, where they decay quickly to the metastable state. Unlike other methods requiring first the 123.6nm lamp light and then the 819nm laser light to excite the atoms, the 215nm excitation only requires one wavelength of light. The 215nm radiation is produced via frequency doubling, by second harmonic generation. The two-photon excitation decays into the metastable state with a 75% branching ratio. While this requires only a laser to produce, the laser needed would not be a relatively inexpensive diode laser but instead a more expensive optical parametric oscillator (OPO) [9, 10] or frequency-quadrupled Ti:S laser.

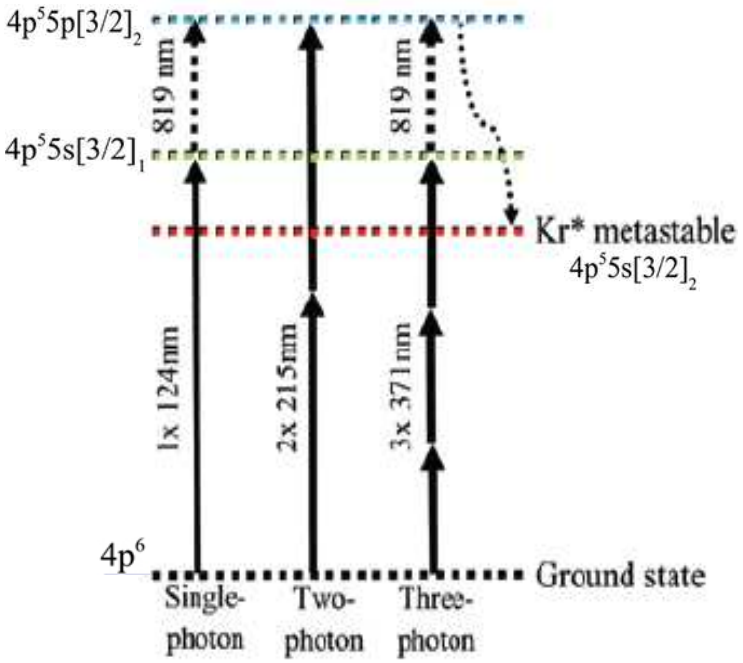

FIG. 3: Excitation options for production of metastable krypton [9].

1.3 OVERVIEW OF THIS THESIS

This thesis examines implementing a newly available commercial lamp at 123.6nm and combining it with an inexpensive 819nm diode laser, eliminating the home-built lamps of previous experiments. To increase the power of the diode laser, a power build-up cavity is incorporated, as no previous papers have explored this option. In Chapter 2 we address the theory behind all-optical excitation, the use of a Fabry-Perot build-up cavity and Doppler-free saturated absorption spectroscopy. In Chapter 3 we document the set-up and apparatus used for this experiment. We discuss the laser configuration chosen for this cavity, the tests done to choose a Fabry-Perot build-up cavity configuration, and characterization of that cavity. In Chapter 4 we discuss the experimental parameters for which one would reasonably expect to see a signal and in Chapter 5 we discuss the project's current status and future prospects for optimization and improvement.

CHAPTER 2

THEORY

2.1 ATOMIC PHYSICS

2.1.1 EXCITATION

Using an all-optical excitation method, a beam of krypton atoms in the metastable $4p^5 5s[3/2]_{J=2}$ level can be be produced at room-temperature. For the first-step of the excitation, from the ground-level $4p^6\ {}^1S_{J=0}$ to the $5s[3/2]_{J=1}$ level, VUV 123.6nm photons are produced by a Resonance RF Powered VUV Krypton Line Source. An 819 nm external cavity diode laser coupled with a symmetric Fabry-Perot build-up cavity is used for the second-step excitation from $5s[3/2]_{J=1}$ to $5p[3/2]_{J=2}$, followed by a spontaneous decay to the $5s[3/2]_{J=2}$ metastable level with an approximately 75% branching ratio (see FIG. 4) [5].

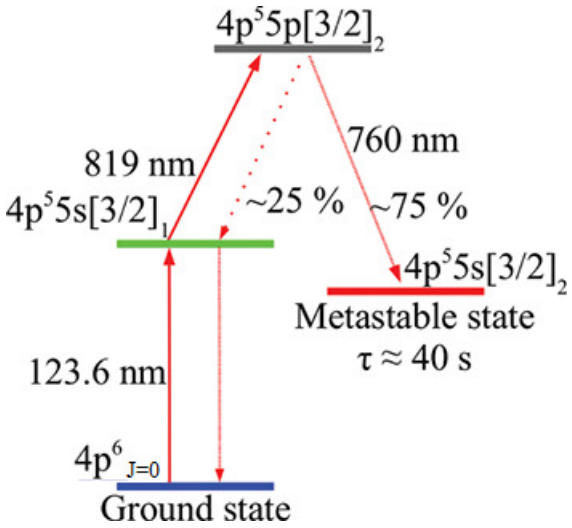

FIG. 4: Krypton optical excitation from the ground state to the metastable state, at J=2 [5].

Rate Equations

A set of differential equations can be used to describe the evolution of the populations of krypton atoms in each state (see FIG.5).

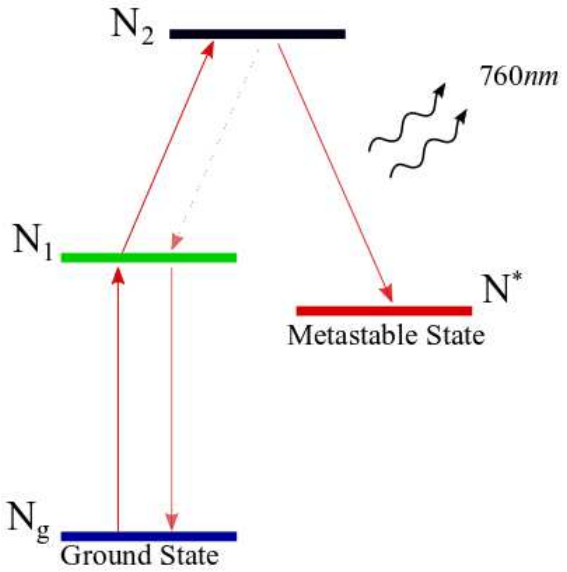

FIG. 5: Populations of atoms in each state, N_g , N_1, N_2, N^*.

Beginning with 100% of the population in ground state, where Γ is the decay rate, R is the scattering rate, and N is the number of atoms in that state,

$$\frac{dN_g}{dt} = -R_{g1}N_g + N_1\Gamma_{1g}. \tag{1}$$

Equation 1 shows that the change in the number of atoms in the ground state over time is equal to the number of atoms excited to the first excited state, plus the number in the N_1 population that decayed back down to the ground state. For the change in the population in N_1 over time, we consider the number lost to N_2 population, plus the gain of de-excited atoms from N_2, minus those lost back to the ground state, plus those gained from the ground state.

$$\frac{dN_1}{dt} = -R_{12}N_1 + N_2\Gamma_{21} - N_1\Gamma_{1g} + R_{g1}N_g. \tag{2}$$

For the change in the population N_2 over time, we have the number gained from

N_1, minus the population lost to N_1, minus the atoms lost to the population in the metastable state,

$$\frac{dN_2}{dt} = R_{12}N_1 - N_2\Gamma_{21} - N_2\Gamma_{2*}. \tag{3}$$

Finally, we get the change in the population of the metastable state in time [11],

$$\frac{dN^*}{dt} = N_2\Gamma_{2*}. \tag{4}$$

Based on the geometry of our set-up, which is currently run as a beam, not a cell, each atom will spend a time t' in the excitation region. We approximate the velocity distribution for the beam to be a Maxwell-Boltzmann distribution.

$$t' = \frac{d}{v} = \frac{d}{\sqrt{\frac{3kT}{m}}}, \tag{5}$$

where time is equal to the distance, d, traveled over the velocity, v, k is the Boltzmann constant, T is the temperature, and m is the mass of a krypton atom.

To solve this set of differential equations we must first find R_{g1} and R_{12}, the excitation rates for both transitions, on resonance. From the ground state to the first excited state using the 123.6nm lamp,

$$R_{g1} = \frac{\Gamma_{1g}s_{g1}}{2\left(s_{g1}+1\right)} \tag{6}$$

where Γ_{1g} is the decay rate for the first transition and s_{g1} is the saturation parameter for the first transition.

$$s_{g1} = \frac{I_R}{I_{satg1}}, \tag{7}$$

where $I_R = 1.01851 \times 10^{-5}\frac{W}{m^2}$ is an estimation from a previous student experiment [11] and I_{satg1} is the saturation intensity of the first transition. The scattering rate for the second transition at 819nm is

$$R_{12} = \frac{\Gamma_{21}s_{12}}{2\left(s_{12}+1\right)} \tag{8}$$

with

$$s_{12} = \frac{I_{819}}{I_{sat12}} \tag{9}$$

where Γ_{21} is the decay rate for the second transition, I_{sat12} is the saturation intensity of the second transition, and I_{819} is the intensity of the Gaussian 819nm laser beam.

The decay rates are known values [12]:

$$\Gamma_{1g} = 3.12 \times 10^8 \mathrm{s}^{-1} = 2\pi(49.66)\mathrm{MHz}$$

$$\Gamma_{21} = 1.1 \times 10^7 \mathrm{s}^{-1} = 2\pi(1.751)\mathrm{MHz}$$

$$\Gamma_{2*} = 3.1 \times 10^7 \mathrm{s}^{-1} = 2\pi(4.934)\mathrm{MHz}$$

To find the intensities needed for the above calculations, where Γ is the decay rate, λ is the wavelength of the laser or lamp, c is the speed of light and h is Planck's constant, we have

$$I_{satg1} = \frac{\pi h c \Gamma_{1g}}{3\lambda_{123}^3} \tag{10}$$

$$I_{sat12} = \frac{\pi h c \Gamma_{21}}{3\lambda_{819}^3} \tag{11}$$

We can express I_{819} in terms of P, the total power of the laser in the build-up cavity, and ω_0, the laser beam waist:

$$I_{819} = \frac{P}{\frac{1}{2}\pi\omega_0^2} \tag{12}$$

To find P we have

$$P = P_{circ} = P_{inc}(\frac{1}{1-\Re}), \tag{13}$$

where P_{inc} is the incoming laser power, P_{circ} is the power circulating in the cavity and $\Re$ is the reflectivity of the cavity mirrors. In summary, our rate equations for estimating the percent of the expected number of atoms in each state after time t' are:

$$\frac{dN_g}{dt} = -R_{g1}N_g + N_1\Gamma_{1g}$$

$$\frac{dN_1}{dt} = -R_{12}N_1 + N_2\Gamma_{21} - N_1\Gamma_{1g} + R_{g1}N_g$$

$$\frac{dN_2}{dt} = R_{12}N_{1g} - N_2\Gamma_{21} - N_2\Gamma_{2*}$$

$$\frac{dN^*}{dt} = N_2\Gamma_{2*}$$

We will solve these equations in Chapter 4 to see what our expected number of metastables will be.

2.2 POWER BUILD-UP CAVITY

Combining a power build-up cavity, or Fabry-Perot cavity, with an 819nm external cavity diode laser (ECDL) allows us to increase the power in the cavity during the second step of the excitation process, which will in turn increase our number of atoms in the metastable state. The Fabry-Perot interferometer is comprised of two partially-transmitting mirrors facing each other. At each mirror surface the light is partially transmitted and reflected. The inner surfaces of the mirrors are highly reflective and the outer surfaces are broadband antireflection coated, this allows for a greater power build-up inside the cavity. The configuration can be chosen to optimize where the location of the strongest portion of the beam is located in the cavity. In FIG. 6 are some of the many configurations to choose from.

The most commonly used configurations are the plane-parallel and the symmetric confocal. The plane-parallel Fabry-Perot is an optical cavity formed by two almost identical, partially-transmitting, flat reflective surfaces or two reflective wedges. The surfaces are positioned parallel to one another and separated some distance L. For resonance in a Fabry-Perot cavity the round-trip phase delay has to be a multiple of 2π.

Neglecting phase shifts on the mirrors upon reflection, for constructive interference within a plane-parallel Fabry-Perot

$$2L = m\lambda \implies \lambda = \frac{2L}{m} \tag{14}$$

where L is the mirror separation, m is an integer and λ is the wavelength and

$$\nu = \frac{c}{\lambda} = \frac{mc}{2L} \tag{15}$$

where ν is the frequency and c is the speed of light. So the free spectral range (FSR) or mode separation is

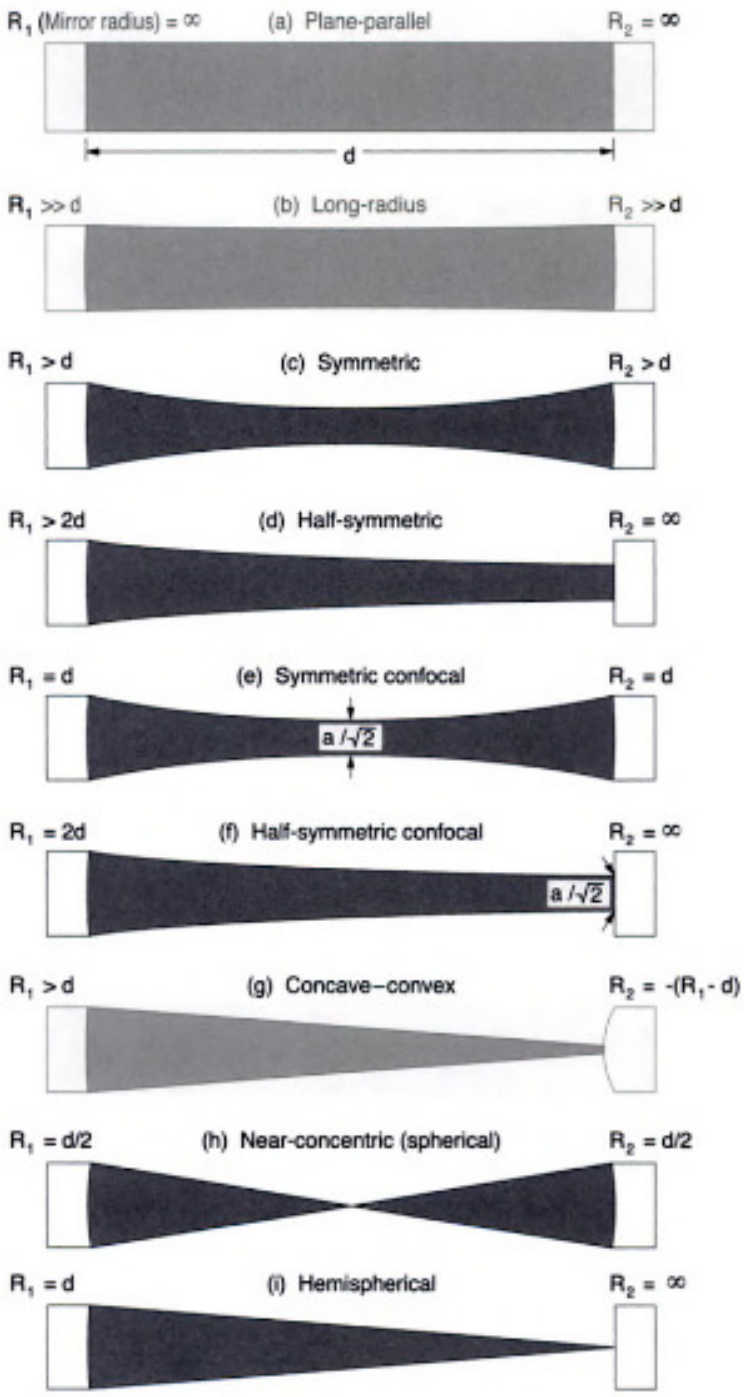

FIG. 6: Examples of possible stable curved mirror cavities [13].

$$FSR = \frac{c}{2L} \tag{16}$$

The downside of this configuration is that it is not as forgiving with respect to how accurately the mirrors need to be placed parallel to one another, in order to achieve the interference fringes we expect to see when aligned properly. The confocal Fabry-Perot is more forgiving and formed by two partially-transmitting, spherical mirrors of the same size and radius of curvature with the separation between the two mirrors equal to their radius of curvature. Taking into account that the spacial modes of a confocal Fabry-Perot are Gaussian, either the resonant frequencies of the transverse modes fall halfway between the longitudinal mode resonances or overlap. So for constructive interference within a confocal Fabry-Perot cavity the mode distance is half of a plane-parallel.

$$FSR = \frac{1}{2}\frac{c}{2L} = \frac{c}{4L} \tag{17}$$

Unlike the plane-parallel case, the symmetric confocal configuration is much more forgiving with respect to aligning the cavity, specifically, it is relatively insensitive to angular alignment.

It is important to note, for all cavity configurations, the sides of the mirrors facing into the cavity are highly reflective and the rear of the mirrors are broadband anti-reflection coated to reduce interference fringes from the back side. The high reflectivity of the mirrors allows for a high Q factor and narrow linewidth, meaning that the cavity is good at storing energy. Using the center frequency of the resonant peak, ν_0, and the linewidth (full width at half maximum), $\triangle\nu$, we can calculate our quality factor, Q.

$$Q = \frac{\nu_0}{\triangle\nu} \tag{18}$$

It is also important to know the finesse, $\mathcal{F}$, of the cavity, or the measure of its ability to resolve closely spaced spectral features. If the Q factor of the cavity is high and the separation is not too large, then the finesse will be high as well. The power in the cavity will increase by an amount proportional to the finesse, so for this experiment a moderately high finesse cavity is desirable.

For the symmetric confocal cavity, where $\Re$ is the reflectivity of the mirrors, we have:

$$\mathcal{F} = \frac{FSR}{\Delta v} = \frac{\pi\sqrt{\Re}}{(1-\Re)} = \frac{c}{4L\Delta v}. \tag{19}$$

For cavities other than the symmetric confocal:

$$\mathcal{F} = \frac{FSR}{\Delta v} = \frac{\pi\sqrt{\Re}}{(1-\Re)} = \frac{c}{2L\Delta v}. \tag{20}$$

To find the power produced inside the cavity we have

$$P_{cavity} = P_{inc}(\frac{1}{1-\Re}) \tag{21}$$

When selecting from the many options available for our application, we must consider stability of the cavity and the size of the beam waist. Stability of different cavities can be mapped using the requirement for two mirrors with two different radii of curvature, R_1, R_2 with $R_1 \neq R_2$ in general, and separated by some distance L, and $0 < g_1 g_2 < 1$ where

$$g_1 = 1 - \frac{L}{R_1} \tag{22}$$

and

$$g_2 = 1 - \frac{L}{R_2} \tag{23}$$

In FIG. 7 we can see the shaded region represents stability. Choosing a configuration that is in the center of the shaded region would be most stable.

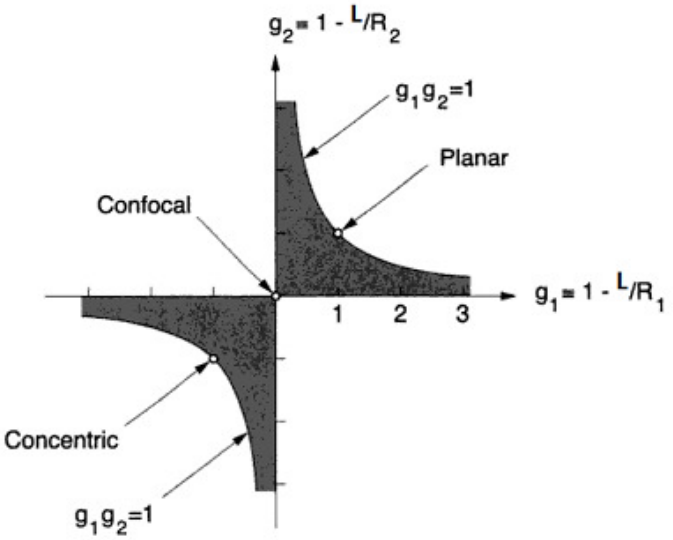

FIG. 7: Stability Diagram for two mirrors with radii of curvature R_1 and R_2 [13].

Notice that although the confocal cavity is considered a stable cavity it is also near the unstable regions and could possibly be tuned out of stability more easily than other configurations. We can see the most stable regions run diagonally between concentric and confocal, and confocal and planar configurations. Therefore, if choosing the most stable option, we would use a symmetric cavity, where the two radii of curvature are the same, $R_1 = R_2 = R$, but greater than the separation between the mirrors, $R > L$, where

$$g_1 = g_2 = 1 - \frac{L}{R} \tag{24}$$

and the minimum beam waist, located at center, is given as

$$\omega_0^2 = \frac{\lambda}{2\pi}[L(2R - L)]^{1/2} \tag{25}$$

and the beam waist at the mirrors are given by

$$\omega_1^2 = \omega_2^2 = \frac{L\lambda}{\pi}[\frac{1}{1 - g^2}]^{1/2}. \tag{26}$$

While the symmetric cavity can provide maximum stability, it does not simultaneously give us the largest possible beam waist in the interaction region. If we use

another configuration we may sacrifice some of the stability in order to get a larger beam waist, but as we want a large beam size to excite as many atoms as possible in our apparatus, this may be a necessary trade-off.

To increase the minimum beam waist and the beam waist at the mirrors we can use the half-symmetric cavity configuration, where one mirror is curved and one mirror is flat, $R_1 = \infty$,and $R_2 > 2L$. This means

$$g_1 = 1 \tag{27}$$

and

$$g_2 = 1 - \frac{L}{R_2} \tag{28}$$

the minimum beam waist is given by

$$\omega_0^2 = \frac{L\lambda}{\pi}[\frac{g}{1-g}]^{1/2} \tag{29}$$

and the beam waist at the curved mirror is given by

$$\omega_2^2 = \frac{L\lambda}{\pi}[\frac{1}{g(1-g)}]^{1/2} \tag{30}$$

One might also consider the long-radius cavity, where $R_1 \approx R_2 \gg L$ due to its large beam waist, given by

$$\omega_0^2 \approx \omega_1^2 \approx \omega_2^2 \approx \frac{L\lambda}{\pi}[\frac{R}{2L}]^{1/2} \tag{31}$$

.

However, stability-wise the long-radius cavity is undesirable. The radii of curvature are so much larger than the separation that we can consider

$$R_1 \approx R \approx \infty,$$

which also means that

$$g_1 \approx g_2 \approx 1.$$

When we look at the stability graph we can see that the characteristics of the long-radius are very close to the plane-parallel cavity, which means the cavity approaches the point of instability. After serious consideration of the options, including what was available in the laboratory, the half-symmetric cavity was chosen to be used in the Fabry-Perot build-up cavity for this stage of the experiment.

In addition to the cavity itself, a focusing lens is needed to couple the laser light straight into the Fabry-Perot cavity. To find the distance, d, to put the focusing lens from the first mirror of the Fabry-Perot cavity:

$$\frac{1}{f} = \frac{1}{f_1} + \frac{1}{f_2} - \frac{d}{f_1 f_2} \tag{32}$$

where f is the focal length of the resulting system, f_1 is the focal length of the focusing lens, and f_2 is the focal length of the first mirror of the Fabry-Perot cavity. Since the focal length of the resulting system needs to be essentially infinite, the equation becomes:

$$0 = \frac{1}{f_1} + \frac{1}{f_2} - \frac{d}{f_1 f_2}$$

and solving for the distance, we find:

$$d = f_1 f_2 (\frac{1}{f_1} + \frac{1}{f_2}) = f_2 + f_1 \tag{33}$$

This calculation determines where we should put the focusing lens before the Fabry-Perot cavity in the experimental set-up.

2.2.1 BREWSTER ANGLED WINDOWS

Options for incorporating the Fabry-Perot cavity into the vacuum system included putting the mirrors inside the vacuum system, or using the mirrors of the cavity as windows on the actual vacuum system, or using windows on the vacuum system at Brewster's angles, so that the Fabry-Perot cavity would sit outside the vacuum system. Putting the mirrors inside the vacuum system was immediately ruled out due

to the inability to adjust the cavity easily. The option of Brewster angled windows was seriously considered (see FIG. 8.)

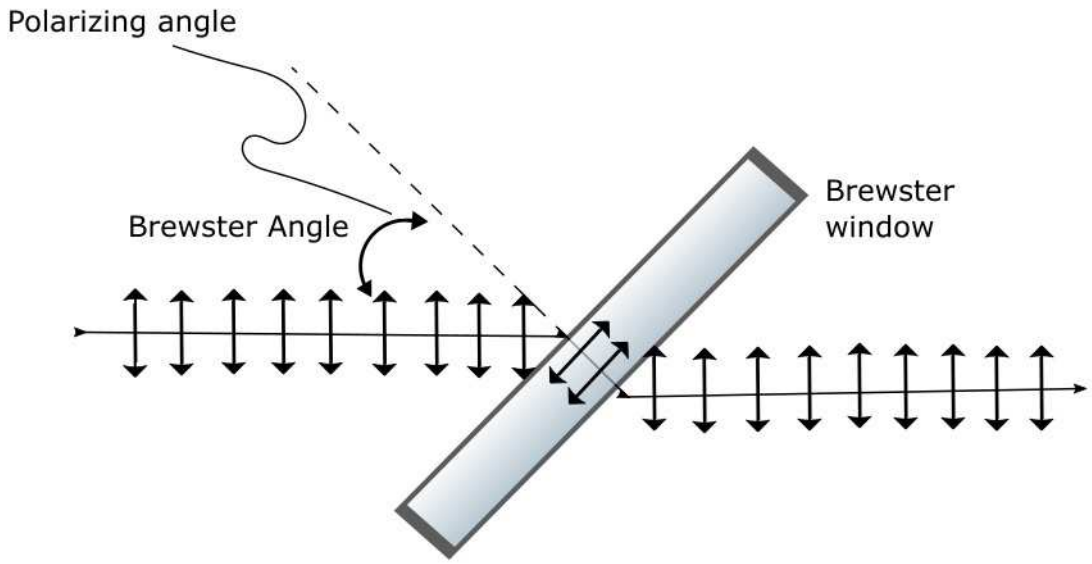

FIG. 8: Brewster angle laser window providing very low reflection loss for light polarized in the plane of the FIG. [13].

Brewster's angle or the polarizing angle is the angle of incidence that perfectly transmits the polarized beam with no reflection from one medium to another [13]. This would allow the laser to be transmitted from air to the vacuum with no loss. It would also allow the Fabry-Perot cavity mirrors to be outside of the vacuum system with full access for adjustment, optimization, and stabilization of the cavity (see FIG. 9).

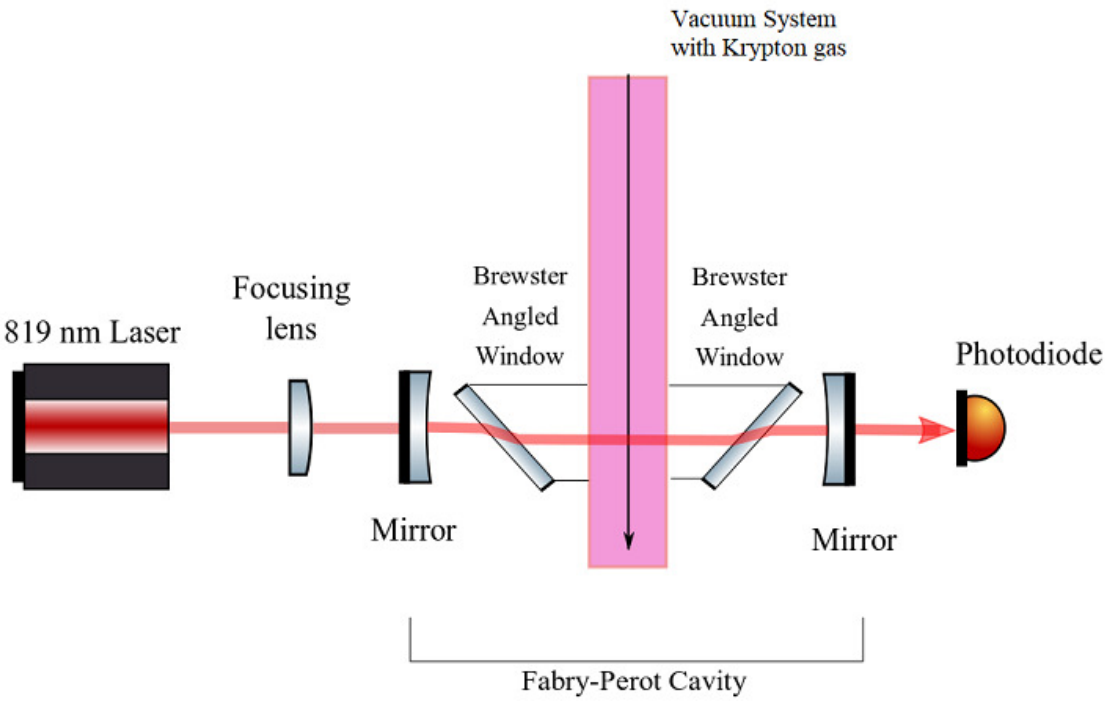

FIG. 9: Brewster angled windows added to a vacuum system using a symmetric cavity.

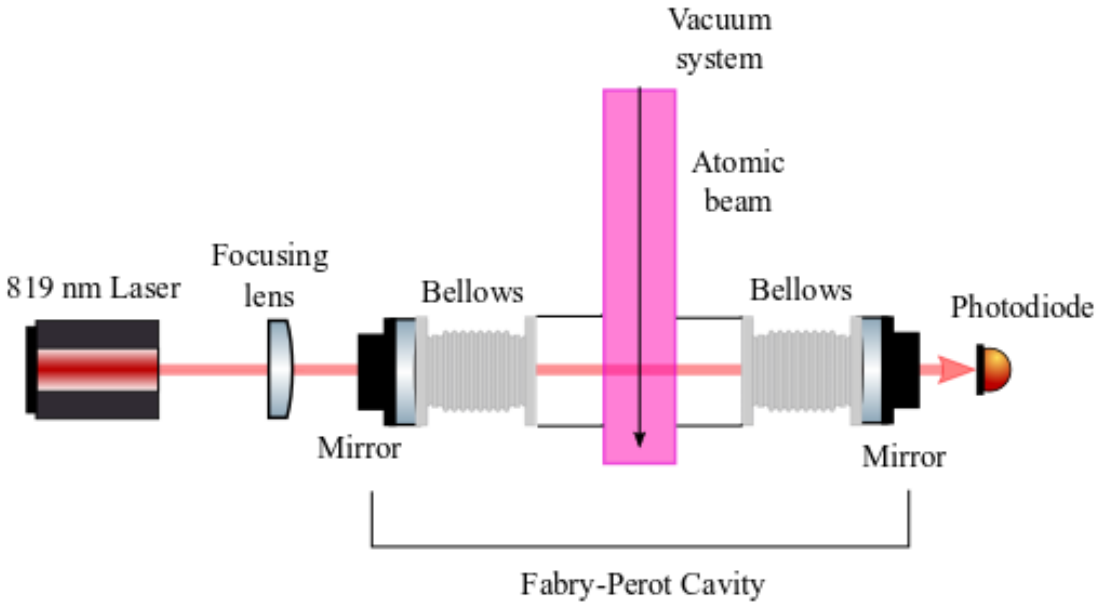

FIG. 10: Cavity mirrors as windows to vacuum system.

With a small tabletop symmetric Fabry-Perot cavity this option was explored and proved to be difficult to get the Brewster angled windows angled properly, due to needing more degrees of freedom than the vacuum apparatus allowed. The test showed that it would be more beneficial to mount the mirrors as the windows of the vacuum system as a first implementation (see FIG. 10), but the Brewster option may be considered again at a later stage.

2.3 DOPPLER-FREE SATURATED ABSORPTION LASER SPECTROSCOPY

Using the Fabry-Perot cavity, the power of the 819 nm laser is increased within the cavity, but in order to get reliable, reproducible data the frequency of the laser needs to be stabilized, or "locked." Using an outside stable frequency reference to stabilize a laser's frequency is the essence of laser locking. The use of atomic absorption lines is a reliable and accurate method since the frequencies of atomic transitions are absolute.

Saturated absorption spectroscopy requires the use of a highly directional, monochromatic or quasi-monochromatic, tunable laser beam. The goal is to excite atoms from lower levels to excited states. The laser beam is split into a strong beam, known as the "pump" beam and a weaker beam, known as the "probe" beam. The beams are sent in opposite directions through a gaseous sample or, more specifically, a vapor cell.

If only the probe beam is sent through the cell, we see an absorption line, which exhibits Doppler broadening (see FIG. 11), or the broadening of spectral lines as a result of the different velocities of the atoms giving rise to different Doppler shifts. This absorption line is called the Doppler profile [14].

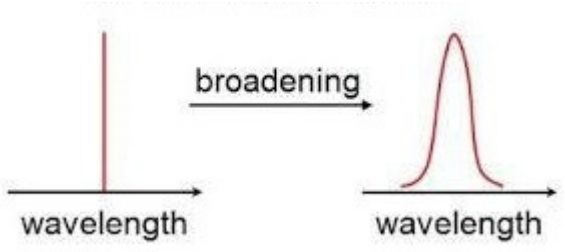

FIG. 11: Example of spectral-line broadening.

If, along with the probe beam, the pump beam is sent through the vapor cell in the opposite direction then a narrow peak is observed in the line, located at the resonant frequency.

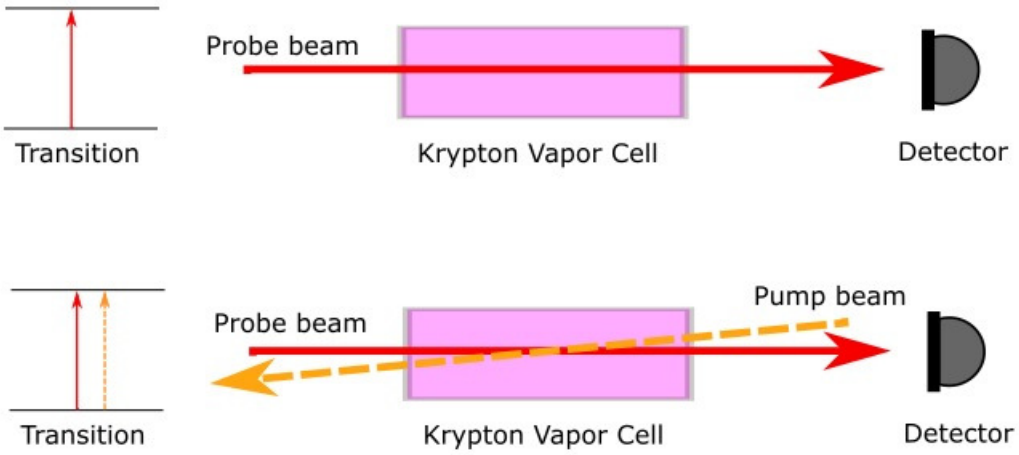

FIG. 12: Sending first the probe beam through a vapor cell, followed by sending both pump beam and probe beam through a vapor cell to produce a peak, or "Lamb-Dip."

The atoms with a zero velocity component along the long axis of the cell see both beams, whereas other atoms see shifted beams due to the Doppler effect. Thus, the atoms with zero longitudinal velocity have the same frequency and since the pump beam has a high intensity, it leads to a high absorption rate, causing less population of ground state atoms for the probe beam to excite. This causes a peak or "Lamb-Dip" to appear in the probe beam's transmission spectra, as shown in FIG. 13 [15].

The peak produced can then be used to lock a laser at a specific wavelength using a number of different methods.

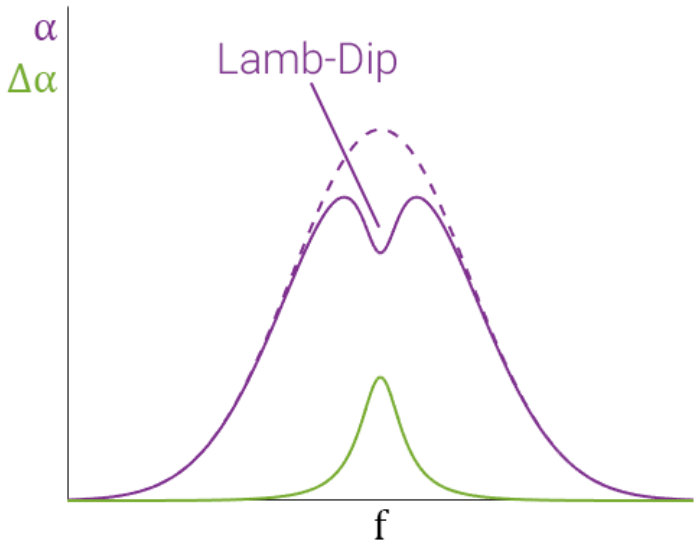

FIG. 13: Absorption in Doppler-Free Spectroscopy without (dashed) and with (solid) pump beam. In green, the absorption difference [16].

CHAPTER 3

EXPERIMENTAL APPARATUS

3.1 EXTERNAL CAVITY DIODE LASERS

Semiconductor lasers make up a large class of lasers that are useful for a variety of applications. Two of the most common cavity configurations are the Littrow and the Littman-Metcalf. Both begin with a laser diode and a collimating lens, the collimated laser light is then incident upon a diffraction grating.

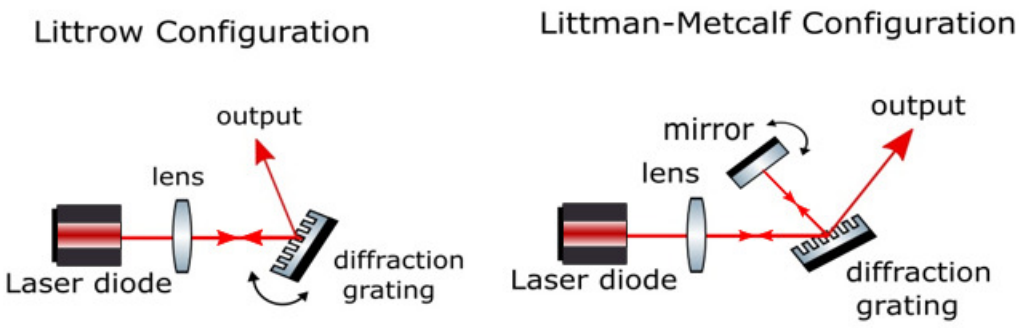

FIG. 14: Littrow and Littman-Metcalf laser configurations [17].

3.1.1 LITTROW

The Littrow configuration is the simplest, since it retro-reflects the first order diffraction back and the zeroth order can be used as the output, minimizing the number of optical elements needed. The downside, however, is that in order to tune it, the grating must be rotated which in turn affects the angle that the zeroth order light comes out.

3.1.2 LITTMAN-METCALF

The Littman-Metcalf configuration was used in this experiment, it uses a mirror along with the grating to select the feedback wavelength. This cavity offers better

selectivity of wavelength and a narrow linewidth. The output is generally the zeroth order since the propagation of the beam is unaffected by the tuning of the wavelength.

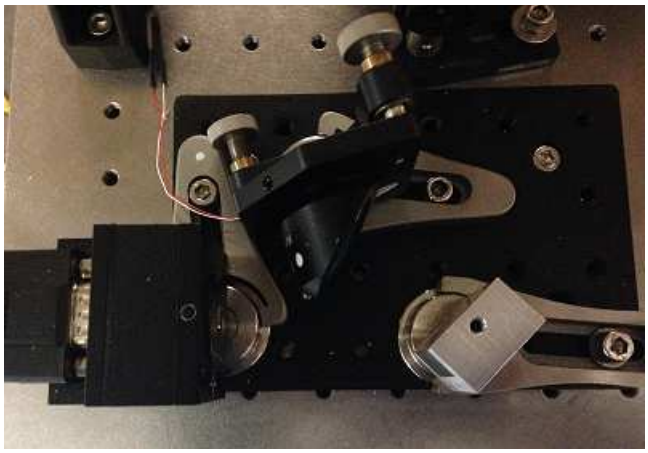

FIG. 15: 819nm External Cavity Laser Diode in Littman-Metcalf configuration built by Hauke Busch.

The final configuration of the ECDL and the saturated absorption spectroscopy optics are shown below:

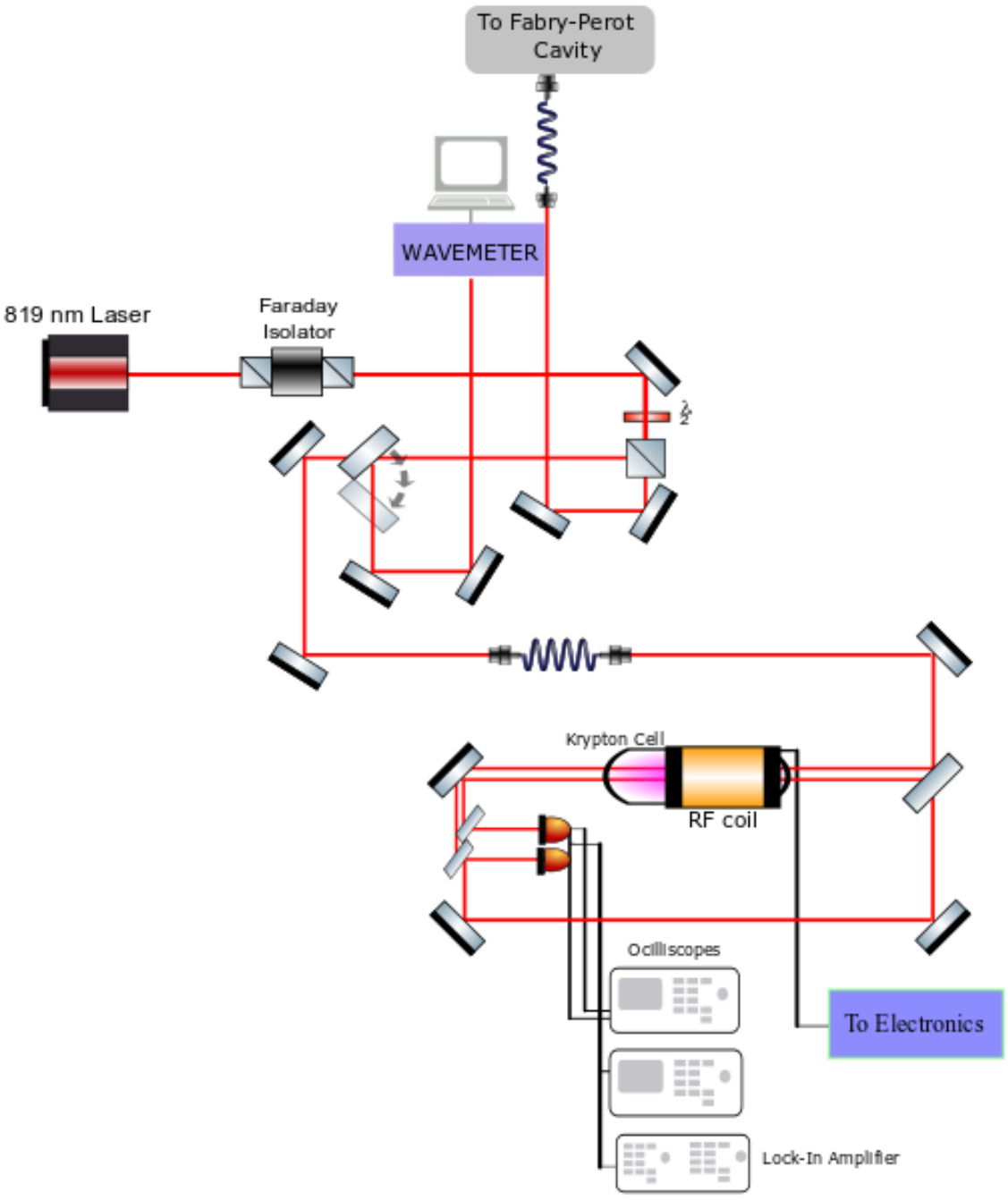

FIG. 16: Laser and saturated absorption schematic.

3.1.3 SATURATED ABSORPTION SPECTROSCOPY

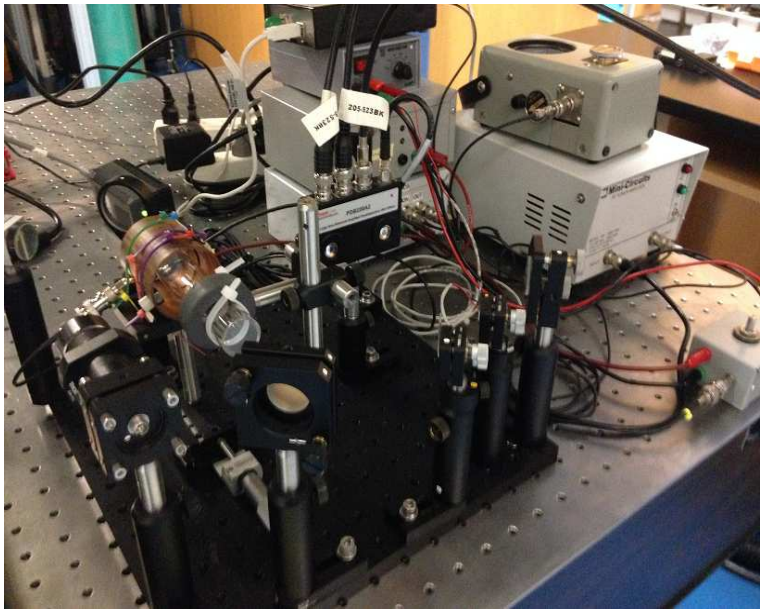

FIG. 17: Saturated Absorption set-up.

In order to see saturated absorption the use of a Lock-In Amplifier, in this case a Stanford Research Systems Model SR844 RF Lock-In Amplifier, was needed. This type of amplifier can assist in solving signal-to-noise issues and allow detection of small signals. The lock-in amplifier uses phase sensitive detection to single out the component of the signal at a specific frequency and phase so that noise signals at other frequencies or random phases are rejected through electronic or software filtering. A high-pass or notch filter then picks off the low frequency noise and allows the signal correlated to the reference signal through. To be more specific, the lock-in amplifier takes the signal from the photodiode and multiplies it by a sine wave at the reference frequency to demodulate the signal, this is known as phase-sensitive detection. When using a reference that is correlated to the signal, the multiplication of the two will give a positive signal and the random noise and the reference will average to zero.

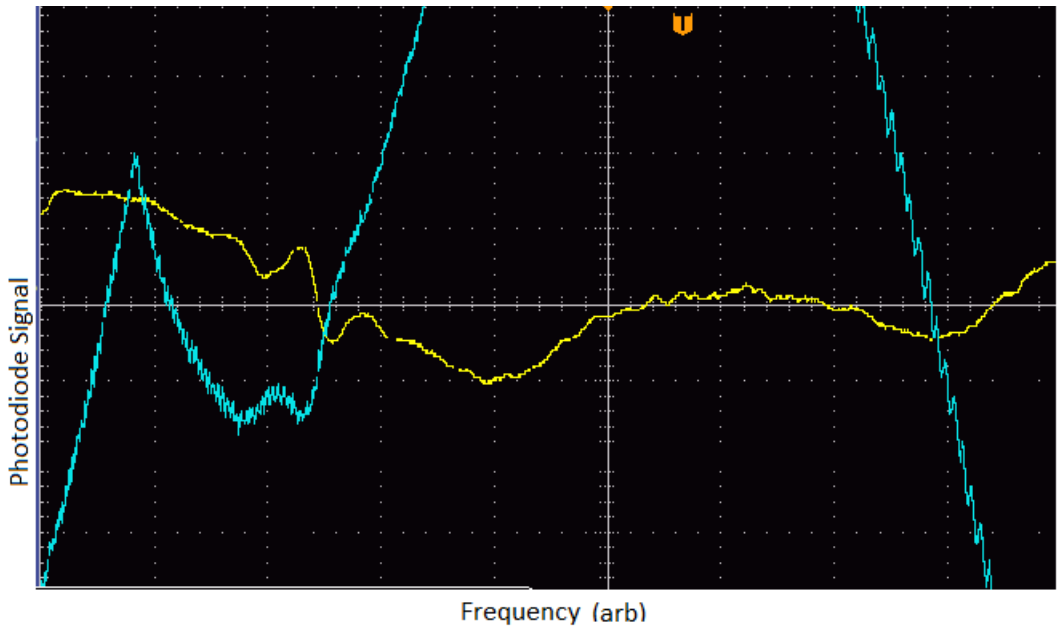

FIG. 18: Saturated absorption peak in blue and lock-in amplifier signal in yellow for 819nm transition.

Using the lock-in amplifier, we were able to see the saturated absorption peak and initially lock the laser. Although, even with the lock-in amplifier it was difficult to see the signal.

The electronics needed for the saturated absorption spectroscopy set-up included a Mini-Circuits RF Frequency Counter, Model UFC-6000, attached to a 1 GHz Voltage-Control Oscillator (VCO), Model z05-1025+, followed by a Mini-Circuits Voltage Variable Attenuator, Model zx73-2500, attached to a Mini-Circuits RF Power Amplifier, Model TIA-1000-IR8, connected to a Thruline Wattmeter, Model 43, connected to the RF coil as shown in FIG. 19.

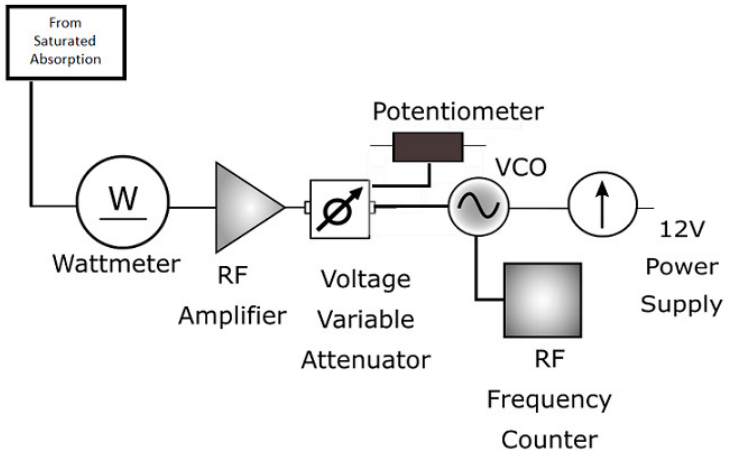

FIG. 19: Electronics for saturated absorption.

3.2 LAMP

The lamp used for the apparatus was the Resonance RF powered Krypton Line Source, model KrLM-LQD12 :

FIG. 20: Resonance RF Powered Krypton Line Source [18].

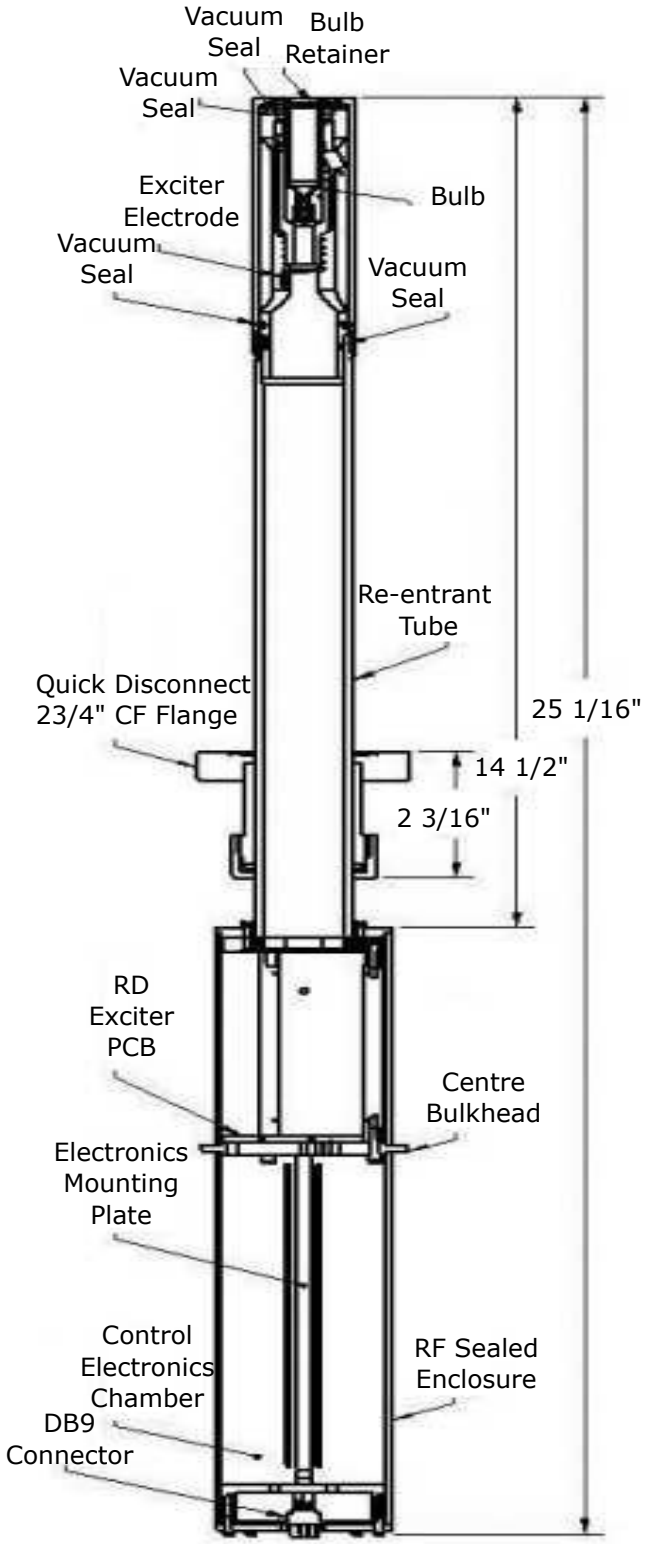

FIG. 21: Schematic of Resonance RF Powered Krypton Line Source from manufacturer [18].

Newly available in 2012, this commercial lamp is a source of 116.5nm and 123.6nm emission. It is a sealed RF source with magnesium fluoride windows, fitted in electromagnetic interference shielded casing. It has a minimum operating life of 1500 hours and max of over 4,000 hours with a typical flux of greater than 3×10^{15} photons per second per steradian.

TABLE 1: RF Powered Line Specifications from manufacturer [18].

Model Number	KrLM-LQD12
Status	in Production
Peak Wavelengths	117,124nm
VUV Flux	3x10^15
Full angle output cone	45 degrees
Bulb window location	10 to 30cm
Window CA	0.8cm
Modulation or pulse	Mod/option
Standard flanges	2.75"CF
Features	Can be close to target deep in vacuum

RF Powered Line Specifications				
	Min.	Avg.	Max.	Unit
Plasma Cavity	20W RF	30x9		Mm ID
Window Material		MgF2		
Drift	0.5@110V max.	0.2	1.0	% per hour
Calibration	Absolute intensity determined by traceable NBS Standard			
Testing	Test Spectrum of entire VUV spectral region performed			
Running Life	1500	>4000		Hours
Case Temperature	100		55	Degrees C
Input Voltage (50-60Hz)	100		250	AC Volts
Optional Pulsed Operation	50		400	Hz

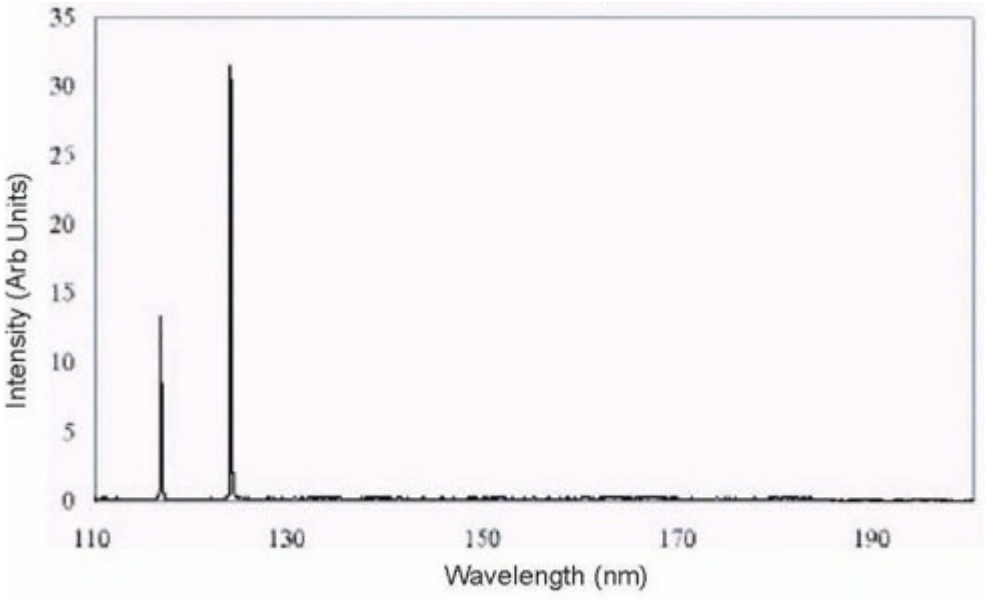

FIG. 22: Kr VUV Line Spectrum provided by Resonance Ltd. [18].

3.3 FABRY-PEROT

To determine which of the Fabry-Perot configurations to use in this experiment several options were tested. First, two 1" flat infrared mirrors were aligned in an attempt to see interference fringes with a camera. This attempt was only successful when the two mirrors were flat against each other; it was extremely difficult to align otherwise, as this cavity falls on the edge of the stable region in FIG. 7, as previously discussed in Chapter 2.

The second test was a symmetric confocal cavity with two convex, highly reflective mirrors with radii of curvature of 10cm. When aligning the cavity, three degrees of freedom were necessary on the second cavity mirror to get results. Once aligned, the cavity was fairly stable and both interference fringes were seen with a camera and transmission peaks were visible with a photodiode and oscilloscope. However, in order for this to be a confocal cavity, it must have a length of 10cm, which would not be long enough to use with the vacuum system. Another issue was that the beam waist would be larger with a different configuration. For two 10cm mirrors, it was only $\sim$ 0.1mm.

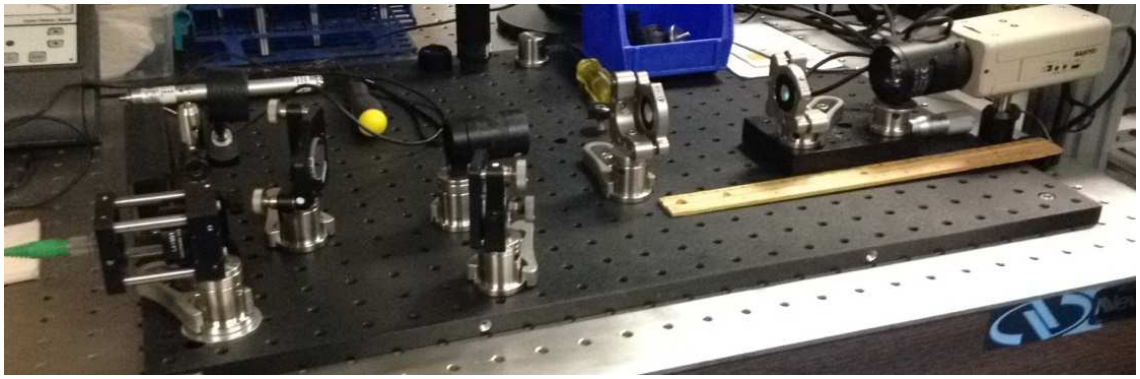

FIG. 23: Fabry-Perot optical breadboard for testing different cavity configurations.

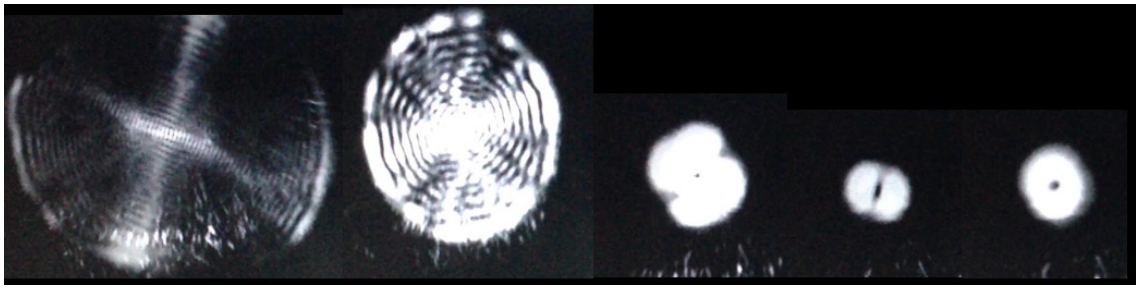

FIG. 24: Interference fringes from Fabry-Perot cavity, coupling into different modes.

After successfully aligning the symmetric cavity, Brewster angled windows were added inside the cavity, but due to the lack of degrees of freedom and space in the cavity, we were unable to get 100% transmission of the light. This deterred usage of Brewster windows in the final configuration of the vacuum chamber.

The next test was aligning a symmetric cavity with two 2" mirrors with 2m radii of curvature. These were tested due to a larger beam waist and considered for use in the vacuum system, but were not used at this time, as commercial vacuum flanges that allow the mirrors to be mounted on the vacuum system were available with 1" size holders only (Future experiments may use custom flanges to accommodate mirrors other than 1 inch diameter). The cavity was aligned to see peaks with a 75cm plano-convex focusing lens, 25cm from the first mirror, and the cavity length, L, set at 50cm and then again at 25cm.

In an effort to ease the alignment process for the next test, the above dimensions

and focusing lens were used, but the mirrors were swapped out one at a time for a 1", $R = 5$m convex mirror and a 1" flat mirror. This half-symmetric cavity was aligned to produce peaks. Since the only cavity length requirement was $R_1 > 2L$, the ability to align the cavity to produce transmission peaks was almost independent of the length of the cavity, which is an advantage over the confocal configuration, whose cavity length must be equal to the radii of curvature of the mirrors. Our vacuum chamber was approximately 42.5cm from one mirror to the other and, had it been a necessity to make that an even 50cm to produce a confocal cavity, it would have been difficult to do space-wise.

After testing the different options available in the laboratory, the Fabry-Perot cavity chosen was the half-symmetric cavity, based on gaining as large a beam waist as possible, while also being in a stable configuration. Other limitations included using what mirrors were already available to us and would fit into the 1" mounts for the vacuum system. The mirrors used were a concave mirror with a 5m radius of curvature and a flat mirror with a theoretically infinite radius of curvature. The mirrors were separated a distance L of approximately 42.5 cm. R_1 was 500cm, R_2 was approximately infinite, and the wavelength was 819nm. For a half symmetric cavity where $R_1 > 2L$,

$$g_1 = 1 - \frac{L}{R_1} = 1 - \frac{42.5}{500} \approx 0.92,$$

and

$$g_2 = 1,$$

the minimum beam waist is given by

$$\omega_0^2 = \frac{L\lambda}{\pi}[\frac{g}{1-g}]^{1/2},$$

$$\omega_0^2 = 0.354\mu\text{m}$$

$$\omega_0 = 0.595\text{mm},$$

and the beam waist at the curved mirror is given by

$$\omega_1^2 = \frac{L\lambda}{\pi}[\frac{1}{g(1-g)}]^{1/2},$$

$$\omega_1^2 = 0.384\mu\text{m},$$

$$\omega_1 = 0.620\text{mm}.$$

Using a plano-convex lens, distance from focusing lens to cavity

$$f_1 = 75\text{cm}$$

and

$f_2 = \frac{R}{2} = \frac{500cm}{2} = 250\text{cm}$. Since the first mirror of the cavity is convex, we have

$$f_2 = -250\text{cm}$$

$$d = f_2 + f_1 = -250 + 75 = -175\text{cm}$$

The mirror should be placed 175cm before the first mirror of the cavity, but it was found in one of the tests that, since it was coupling into so many modes and none were degenerate, it would work at 25cm. Due to lack of space, this distance was used in the final configuration of the apparatus.

3.3.1 CHARACTERIZING THE CAVITY

Once the chosen half-symmetric cavity is aligned, we see transmission peaks, as seen in FIG. 25. We now begin to characterize by calculating the free spectral range of our cavity using Equation 16:

$$FSR = \frac{c}{2L} = \frac{3 \times 10^8}{2 \times .425m} = 353\text{MHz}$$

and using equation 21, where $\Re = .98$ is the reflectivity, the finesse of the cavity is

$$\mathcal{F} = \frac{\pi\sqrt{\Re}}{(1-\Re)} = 156.$$

Using the reflectivity of the cavity mirrors, the power circulating inside the cavity can be calculated as well, using equation 21:

$$P_{circ} = P_{inc}(\frac{1}{1-\Re}) = 2.46mW * 50 = 0.123\text{W}.$$

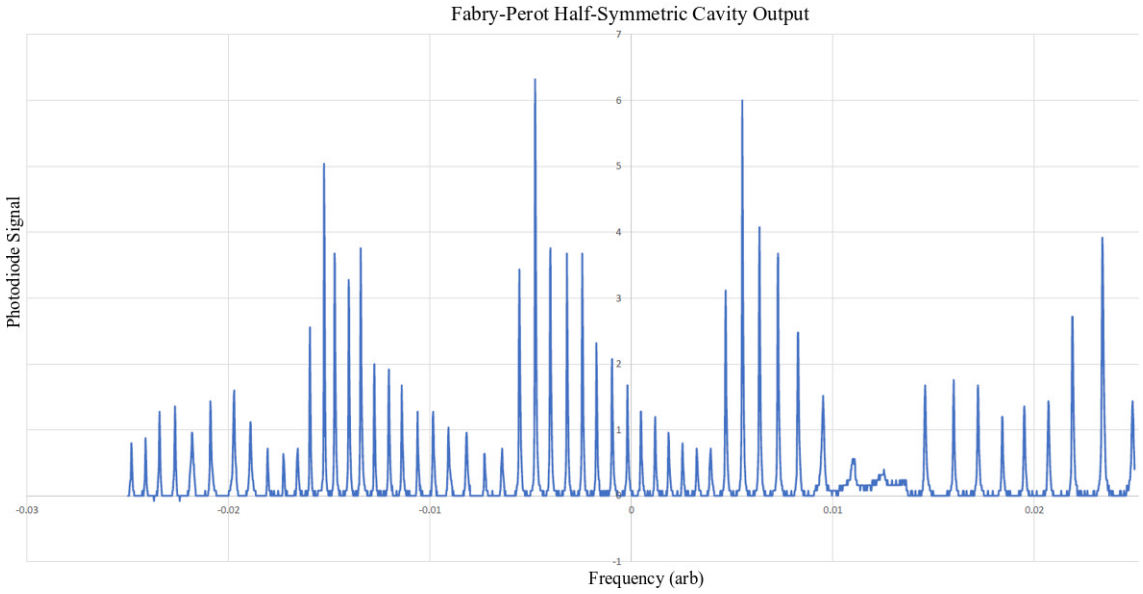

FIG. 25: Output of Fabry-Perot Half-Symmetric cavity.

3.4 VACUUM SYSTEM

The final configuration of the vacuum system is pictured below, followed by a table including the part numbers and descriptions of each piece of equipments' purpose in the experiment.

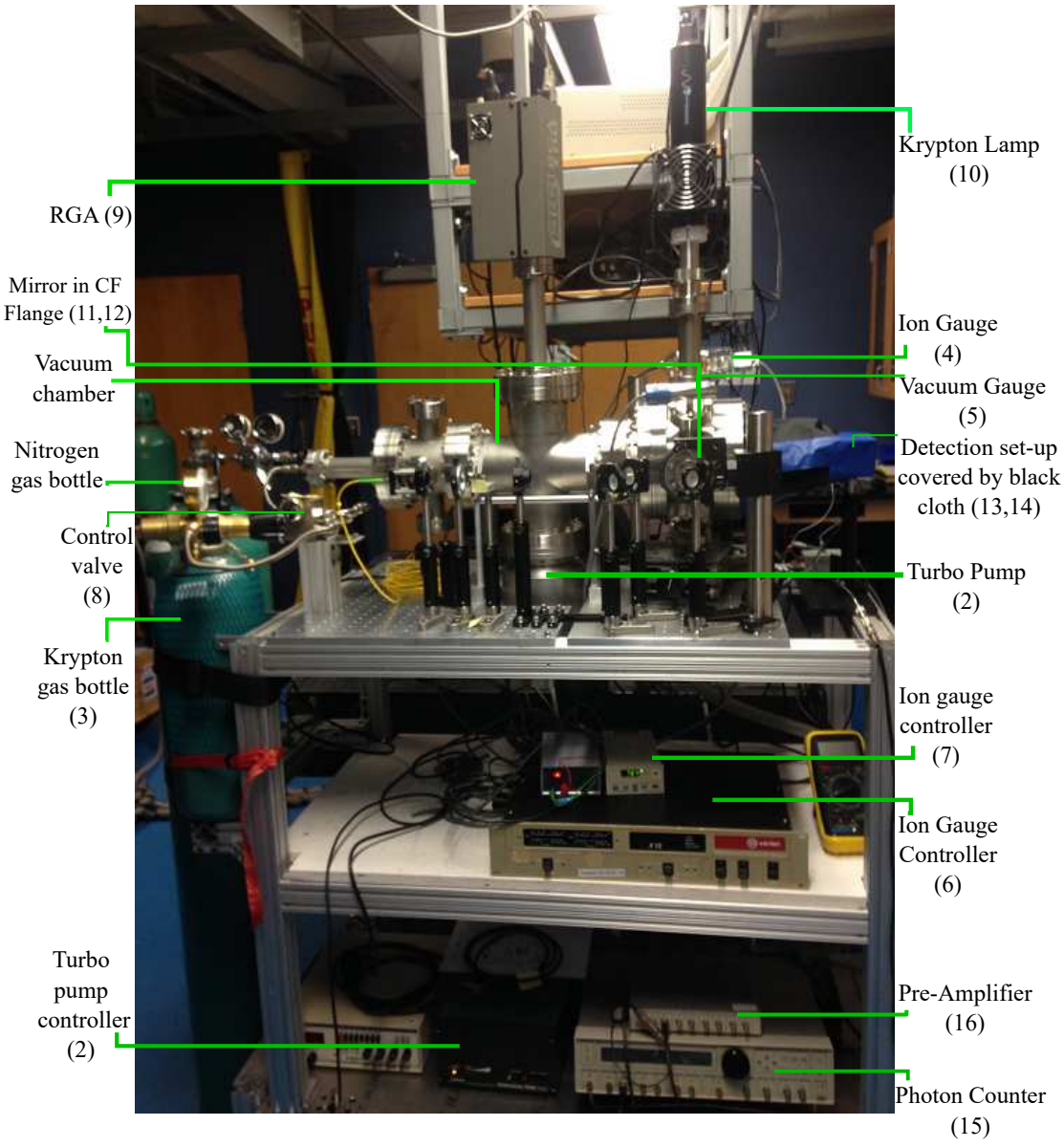

FIG. 26: Vacuum system final configuration.

TABLE 2: Table of Equipment for Vacuum System Final Configuration.

#	Equipment	Description
1	Dry Scroll Vacuum Pump, Edwards XDS 10	(not pictured) - Pumps out the chamber to lower the pressure.
2	Leybold Vacuum Turbo pump with Turbo-Drive TD20 Classic	Assists the scroll pump or roughing pump in bringing the chamber down in pressure.
3	Krypton Gas Bottle	
4	Huntington IK-100 Ion Gauge	Gives pressure in Vacuum chamber from Torr and below. 10^{-4}
5	Granville Phillips 275238 Convectron Gauge Vacuum Pressure Sensor Unit	Gives the pressure in the vacuum chamber down to milliTorr.
6	Varian 880 Vacuum Ion Gauge Controller	Controls Huntington Ion Gauge.
7	Granville-Phillips Series 375 Convectron Vacuum Gauge Controller	Controls Granville Phillips 275238 Convectron Gauge Vacuum Pressure Sensor Unit.
8	Control Valve - 216 Servo Driven Valve Assembly Model No. 4682 B7	Controls Krypton gas entering chamber.
9	RGA100-Residual Gas Analyzer	Analyzes pressure and contents of vacuum chamber.
10	Resonance RF powered Krypton Line Source, model KrLM-LQD12	Krypton Lamp at 123.6nm.
11	1'' Mirrors: R=5m and flat (R=infinity)	Mirrors for Fabry-Perot cavity
12	2.75'' CF Flange with 0.75'' View Diameter - VPCH12-FL TP016881063	Holds mirrors for Fabry-Perot cavity and attaches them to the vacuum system as windows
13	Thorlabs FB760-10 760nm Bandpass Filter	Filters out light other than 760nm light.
14	Hamamatsu R928 Photomultiplier Tube (PMT) with HC123-01 Base and Power Supply	Detects incoming photons.
15	SRS SR400 Two Channel Gated Photon Counter	Allows us to count photons detected by PMT.
16	SRS Stanford Research Systems-Model SR445A - Four Channel, DC to 350MHz Amplifier	Amplifies signal from PMT.

3.5 DETECTION

3.5.1 LAMP TEST

The RF powered krypton lamp was tested first using a Model 470 DeTech Channeltron, with an SRS SR400 Two Channel Gated Photon Counter and SRS Stanford Research Systems-Model SR445A - Four Channel, DC to 350MHz Amplifier and High Voltage power supply, to ensure that the lamp was indeed putting out enough light to perform the experiment. Due to how new this commercial lamp was, the specifications were sparse. It was unknown if the lamp had a shelf life. It was known, however, that it has a running life of a minimum of 1500 hours, but it was sitting on a shelf for a few years after its last use.

To test the lamp, an 8" flange with a port clamp mount attached to the inside, on which the channeltron was attached, was added to vacuum chamber. A pre-amplifier and photon counter were added as well to count the number of photons reaching the channeltron once the lamp was turned on.

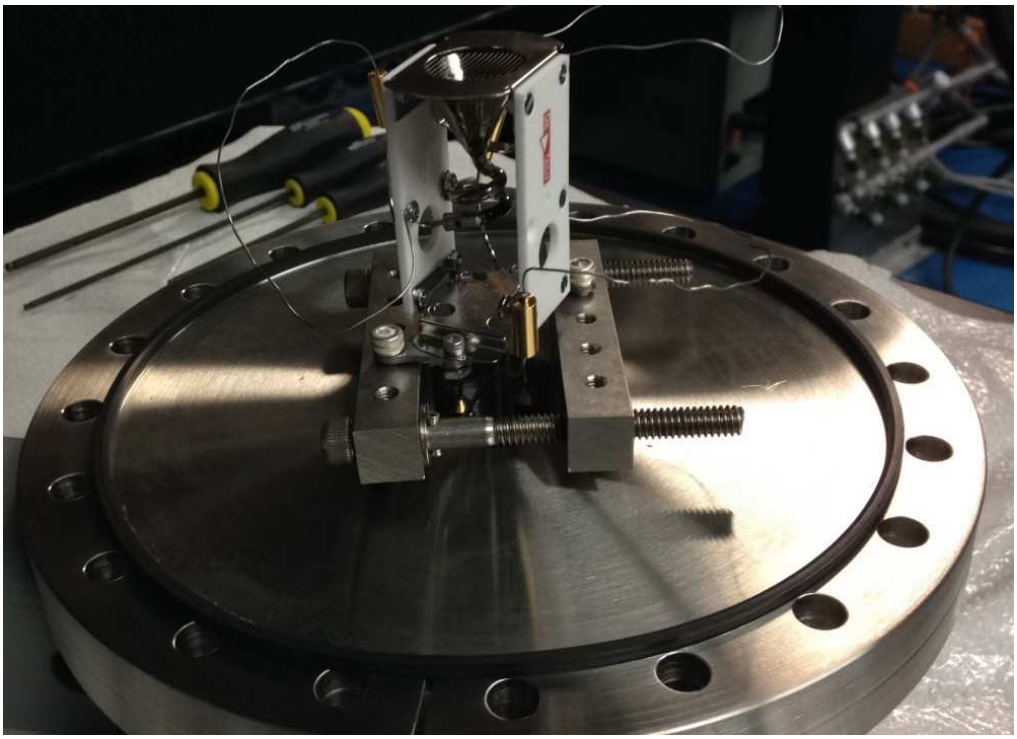

FIG. 27: 8" flange with port clamp mount and channeltron attached before being added to vacuum system.

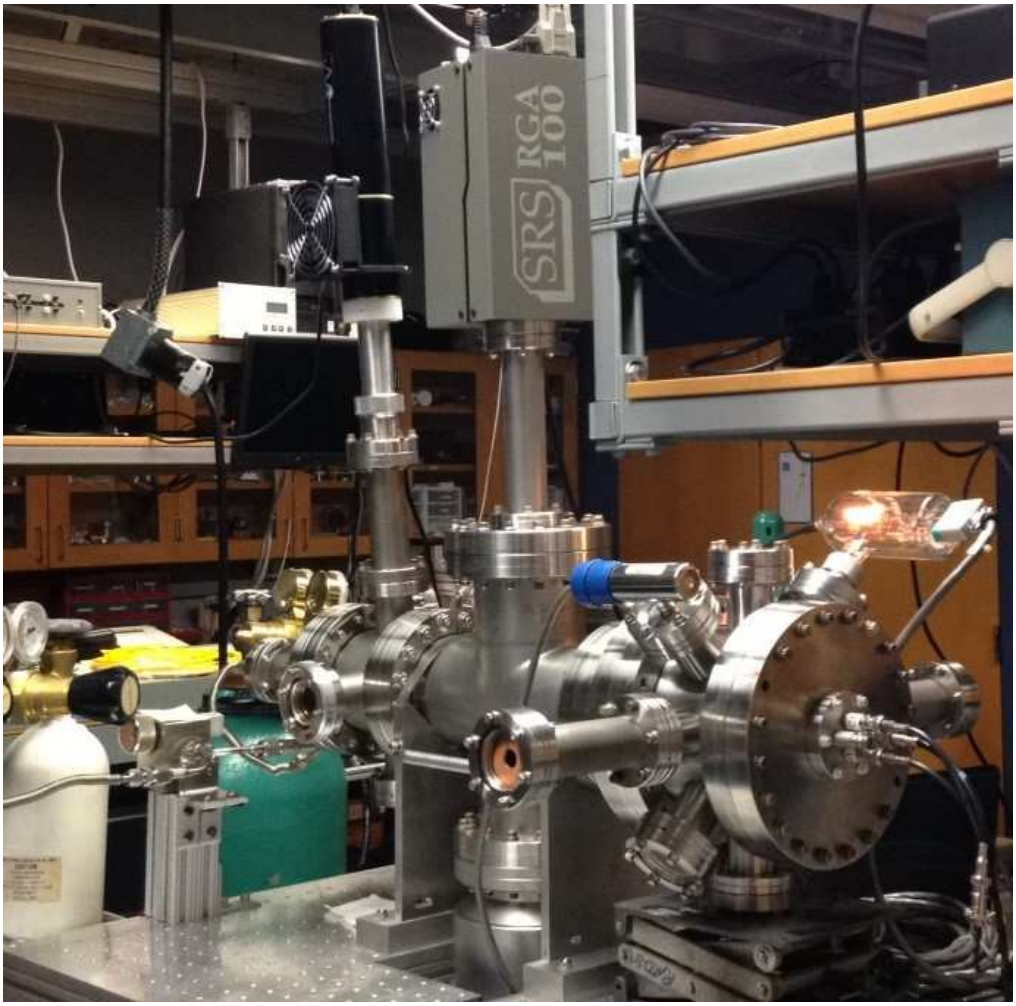

FIG. 28: Vacuum chamber set-up for lamp test.

Before beginning the first test, the discriminator level was determined by running the channeltron without the lamp on and choosing a setting to exclude as much of the noise as possible. The lamp was then run for 30 minutes and then shut off. The number of photon counts was ~ 250 for one second with the lamp off and no krypton gas added. The lamp was then turned on and the number of counts spiked to $\sim 5,000$ for one second (these are UV photons detected by the channeltron). When the lamp was then shut off again, the number of counts dropped to 108 for one second. This indicated that the lamp was indeed working.

A second test was performed with krypton present to look for resonant scattering. With the lamp turned on, $\sim 3,000$ counts were seen. Next, krypton gas was added and the number of counts spiked to $\sim 450,000$. Next, the krypton gas was pumped

away and nitrogen gas was added. The number of counts spiked to 150, 000. In order to draw a more quantitative conclusion, this test will be repeated in the future.

3.5.2 760 NM BANDPASS FILTER

A Thorlabs 1" FB760-10 bandpass filter was used as the last step before collection at the photomultiplier tube. It was mounted in a 1" collimating tube near the window of the vacuum system. This lens transmits at minimum 50% of the 760nm light and blocks 200-1200nm, as shown in FIG. 29. This allows us to better detect the 760nm light produced in the transition to the metastable state by the Kr atoms. For every atom transitioning from $5p[3/2]_{J=2}$ to the metastable state, a 760nm photon is produced, but that signal could be lost amidst the other wavelengths of light going to the photomultiplier tube, so the filter allows us to block the other wavelengths and only see the signal for the 760nm light.

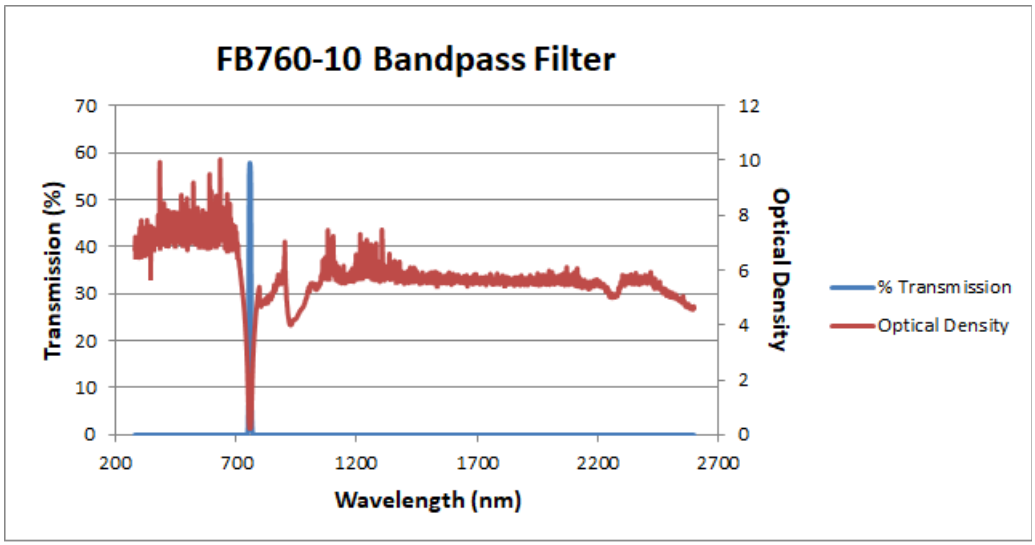

FIG. 29: Transmission and optical density data for Thorlabs FB760-10 bandpass filter, from the manufacturer.

3.5.3 PHOTOMULTIPLIER TUBE AND PHOTON COUNTING

Following the collimating lens and 760nm bandpass filter in the collimating tube, the photons were detected by a Hamamatsu R928 Photomultiplier Tube (PMT),

as shown in FIG. 30, with HC123-01 Base and Power Supply, connected to an SRS SR400 Two Channel Gated Photon Counter and an SRS Stanford Research Systems-Model SR445A - Four Channel, DC to 350MHz pre-amplifier.

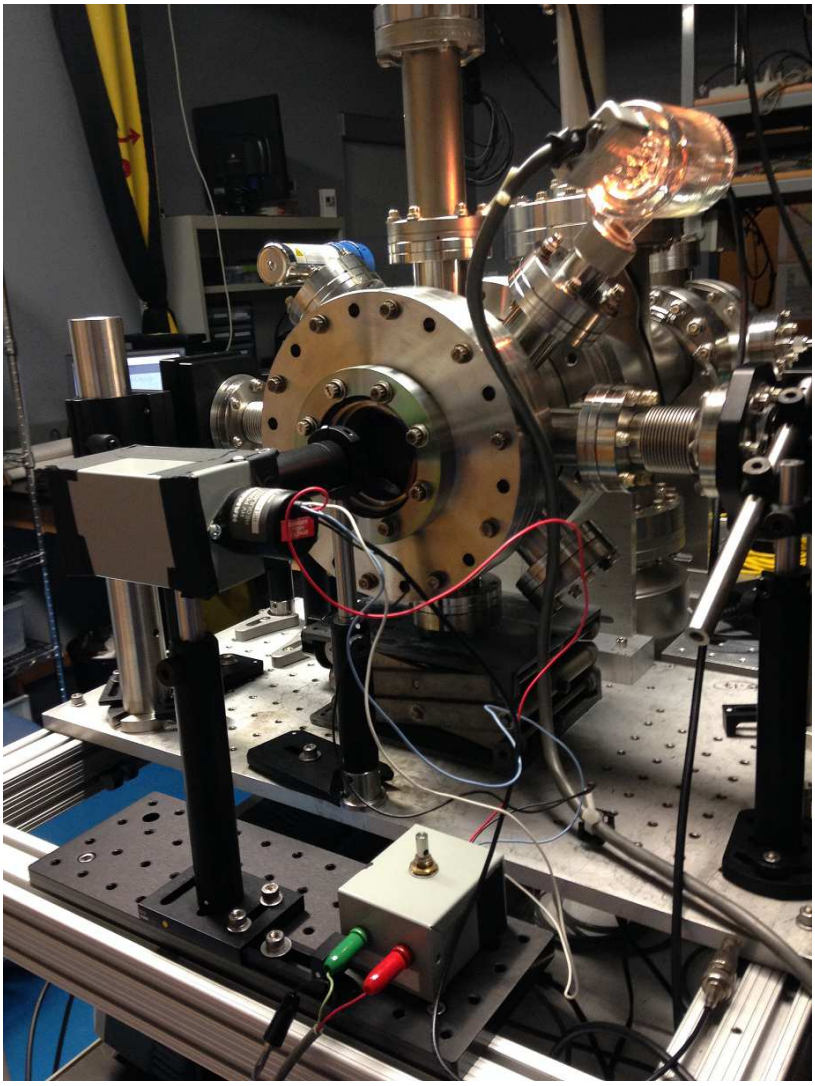

FIG. 30: Photomultiplier tube set-up at the end of the vacuum chamber.

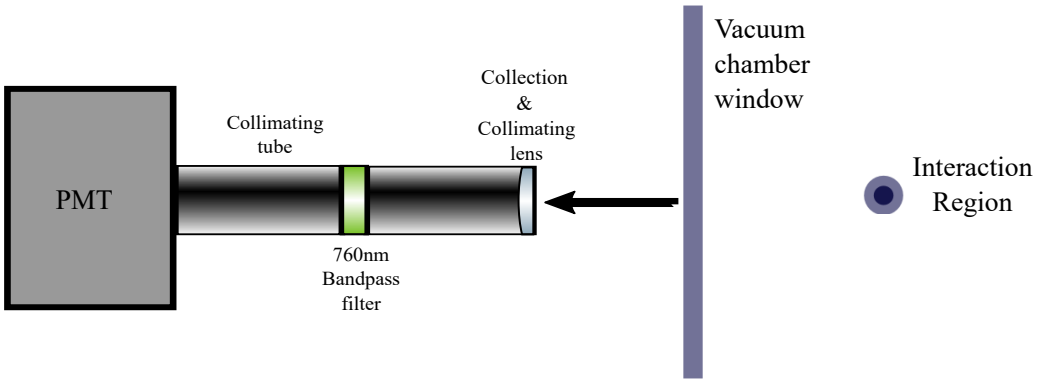

FIG. 31: Detection set-up for vacuum system.

Before any data collection, it was noticed that the output signal of the PMT was ringing, which means there were reflections from the input to the pre-amplifier. Ringing can cause multiple counts from a single photon, which would skew our data collection, so an adjustable snubber cable was added to cancel out any anode signal ringing (see FIG. 32). The snubber cable can be adjusted from 0 to 50 Ohms and allows us to tune it until we see the ringing signal inverted thereby reducing the chance of photons being double counted.

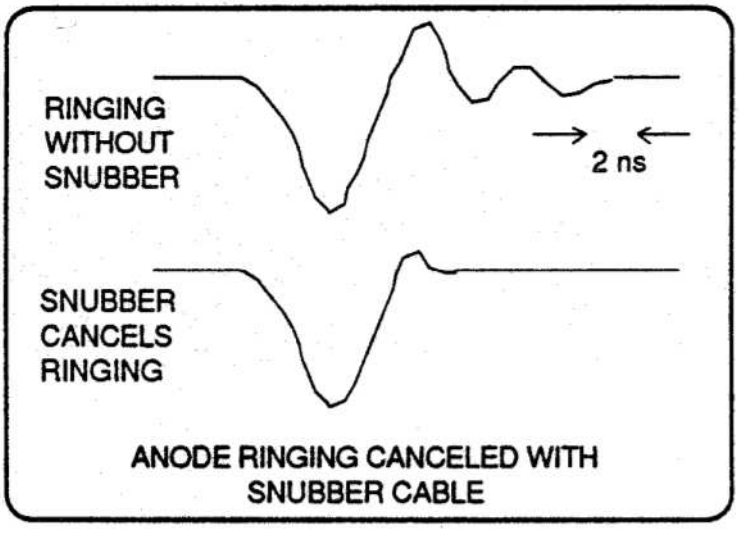

FIG. 32: Snubber cable effect on anode ringing [19].

CHAPTER 4

FEASIBILITY ANALYSIS

4.1 CALCULATIONS

To estimate if our current set-up (without several upgrades planned for the near future to increase our detection efficiency and reduce noise) has the possibility of seeing a signal from the production of metastable Kr, we can begin by using the equations from Chapter 2 to solve for the intensities, saturation parameters and scattering rates:

To determine the Gaussian intensity of the 819nm laser, we have

$$I_{819} = \frac{P_{circ}}{\frac{1}{2} \times \pi \times {\omega_0}^2} = 31,302 \frac{\mathrm{W}}{\mathrm{m}^2} = 3.13 \frac{\mathrm{W}}{\mathrm{cm}^2}$$

where $P_{circ} = 0.123\mathrm{W}$ is the power circulating inside the cavity, $P_{inc} = 2.46 \times 10^{-3}\mathrm{W}$ is the incoming laser power, and ω_0 is the beam waist. To determine the saturation intensity for the 819nm laser, we have

$$I_{\mathrm{sat12}} = \frac{\pi}{3}\left(\frac{hc\Gamma_{21}}{{\lambda_{819}}^3}\right) = 4.16 \frac{\mathrm{W}}{\mathrm{m}^2} = 4.16 \times 10^{-4} \frac{\mathrm{W}}{\mathrm{cm}^2}$$

where $\Gamma_{21} = 1.1 \times 10^7 \mathrm{s}^{-1}$ and $\lambda_{819} = 819 \times 10^{-9}\mathrm{m}$. To find the saturation parameter and scattering rate for the 819nm laser, we have

$$s_{12} = \frac{I_{819}}{I_{\mathrm{sat12}}} = 234,650$$

$$R_{12} = \frac{\Gamma_{21} s_{12}}{2\left(s_{12}+1\right)} = 5.50 \times 10^6 \mathrm{s}^{-1}$$

To find the saturation intensity for the krypton lamp at 123.6nm, we have

$$I_{\mathrm{satg1}} = \frac{\pi}{3}\left(\frac{hc\Gamma_{1g}}{{\lambda_{123}}^3}\right) = 34,902 \frac{\mathrm{W}}{\mathrm{m}^2} = 3.49 \frac{\mathrm{W}}{\mathrm{cm}^2}$$

where $\Gamma_{1g} = 3.12 \times 10^8 \mathrm{s}^{-1}$ and $\lambda_{123} = 123.6 \times 10^{-9}\mathrm{m}$. To find the saturation parameter and scattering rate for the lamp, we have

$$s_{g1} = \frac{I_R}{I_{\text{satg1}}} = 2.92 \times 10^{-10}$$

$$R_{g1} = \frac{\Gamma_{1g} s_{g1}}{2\left(s_{g1}+1\right)} = 0.0455\text{s}^{-1}$$

Next, we will need to know the minimum amount of time an atom may spend in the interaction region, t' with $m = 1.39 \times 10^{-25}$kg, $k = 1.38 \times 10^{-23}$m kg s K^{-1}, $d = 2 \times \omega_0$, $\omega_0 = 0.5 \times 10^{-3}$m is the beam waist and $T = 294.3$K.

$$t' = \frac{d}{\sqrt{\frac{3kT}{m}}} = 3.38 \times 10^{-6}\text{s}$$

Using the solutions for our scattering rates and t', we can solve our rate equations repeated below, beginning with 100% of the krypton atoms in the ground state at time $t = 0$s.

$$\frac{dN_g}{dt} = -R_{g1}N_g + N_1\Gamma_{1g}$$

$$\frac{dN_1}{dt} = -R_{12}N_1 + N_2\Gamma_{21} - N_1\Gamma_{1g} + R_{g1}N_g$$

$$\frac{dN_2}{dt} = R_{12}N_{1g} - N_2\Gamma_{21} - N_2\Gamma_{2*}$$

$$\frac{dN^*}{dt} = N_2\Gamma_{2*}$$

From these equations we obtain the fraction of atoms in each state after time t',

$$N_g \Rightarrow 1$$

$$N_1 \Rightarrow 1.44 \times 10^{-10}$$

$$N_2 \Rightarrow 1.89 \times 10^{-11}$$

$$N^* \Rightarrow 1.96 \times 10^{-9}$$

after time t'. The time evolution of the populations is plotted in FIGS. 33, 34, 35 and 36.

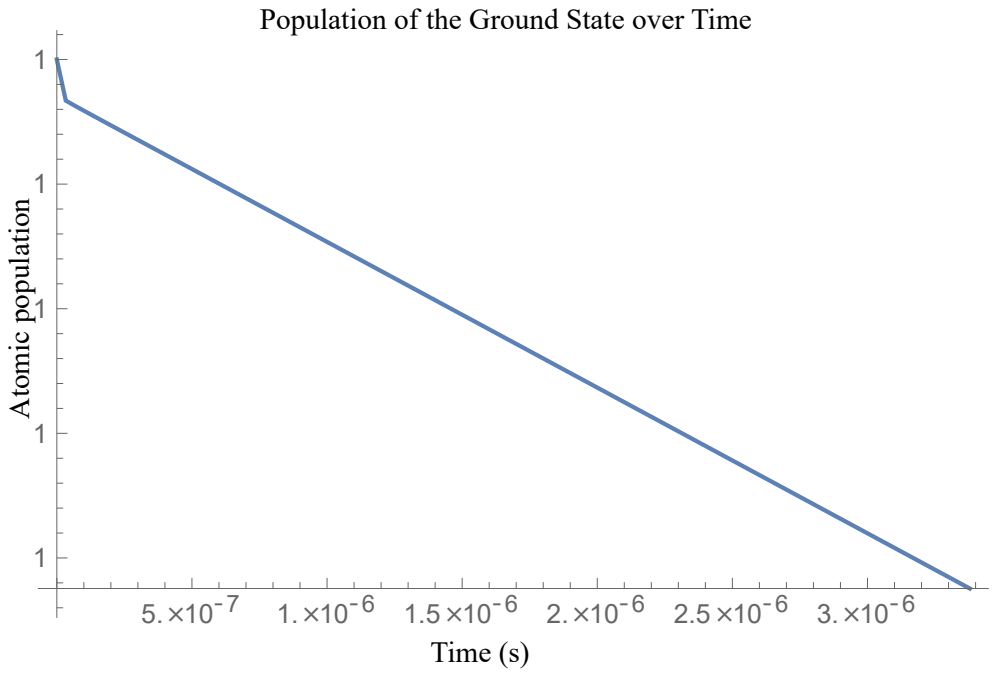

FIG. 33: Graph of the population of the ground state over time, t'.

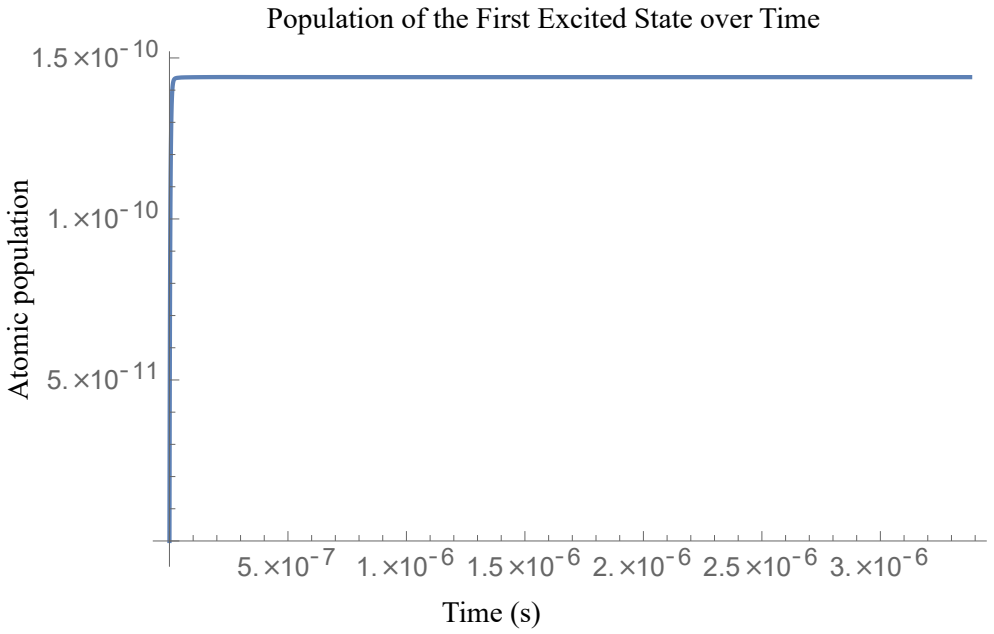

FIG. 34: Graph of the population of the first excited state over time, t'.

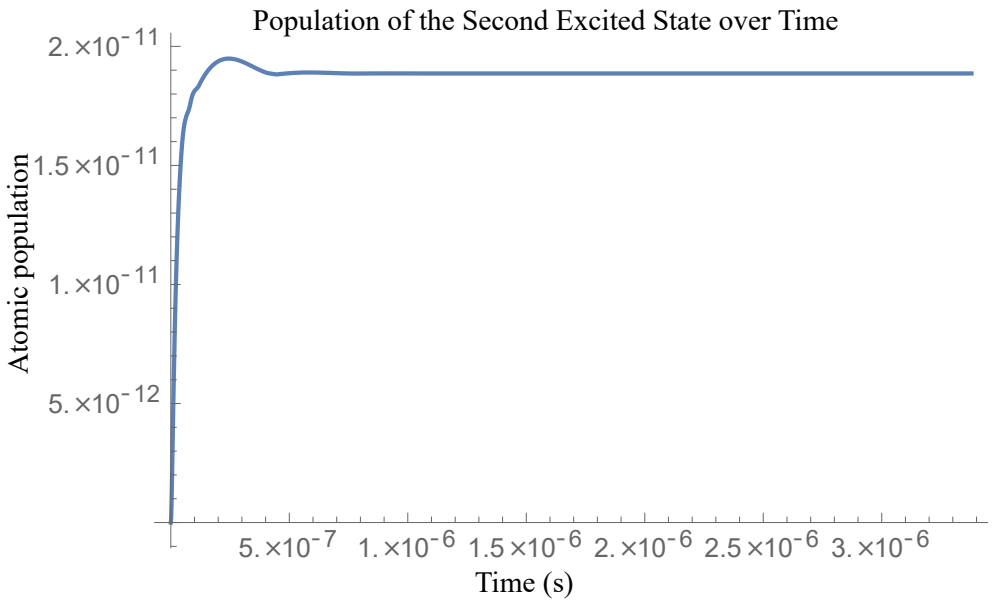

FIG. 35: Graph of the population of the second excited state over time, t'.

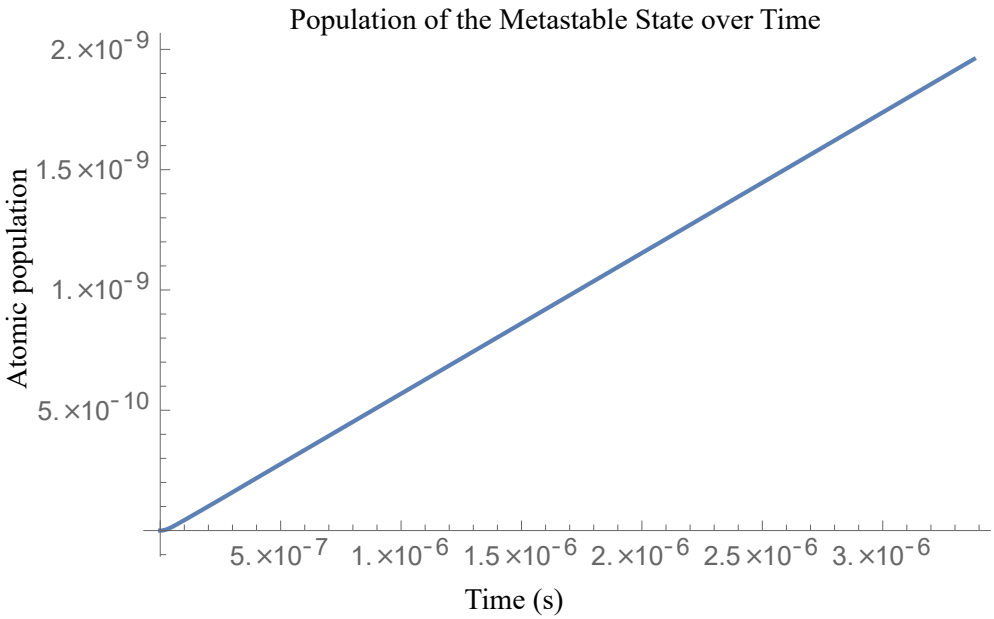

FIG. 36: Graph of the population of the metastable state over time, t'.

Calculating the volume, V, of the interaction region,

$$V = \pi \times r^2 \times L = 6.28 \times 10^{-9}\text{m}^3$$

where $r = 0.5 \times 10^{-3}$m and $L = 0.008$m.

Using our calculations of the volume and the current pressure in the vacuum chamber, $p = 5 \times 10^{-6}$Torr (666.612×10^{-6}Pa), we can find the number of atoms in the interaction region:

$$N = \frac{pV}{kT} = 1.03 \times 10^9\text{atoms}$$

In terms of pressure (in units of Pa):

$$N = 1.55 \times 10^{12}p,$$

where p is pressure. Next we'll need to find the number of 760nm photon counts per second from the PMT we expect to see as each 760nm photon indicates a metastable Kr atom has been created. However, first we need to find the number of 760nm photons produced per second in the interaction region:

photons per second = (probability of atoms in N^*)$\times$(Number of atoms in interaction region)$/t'$

$$\frac{\#photons}{s} = \frac{(1.96 \times 10^{-9})(1.03 \times 10^9\text{atoms})}{3.38 \times 10^{-6}s} = 597,907\text{photons/s}$$

In terms of pressure:

$$\frac{\#photons}{s} = \frac{(1.96 \times 10^{-9})(1.55 * \times 10^{12}p)}{3.38 \times 10^{-6}\text{s}} = 8.97 \times 10^8 p$$

where p is pressure. We'll also need to find the area of the solid angle of scattered photons that make it to the collection/collimating lens of the detection apparatus:

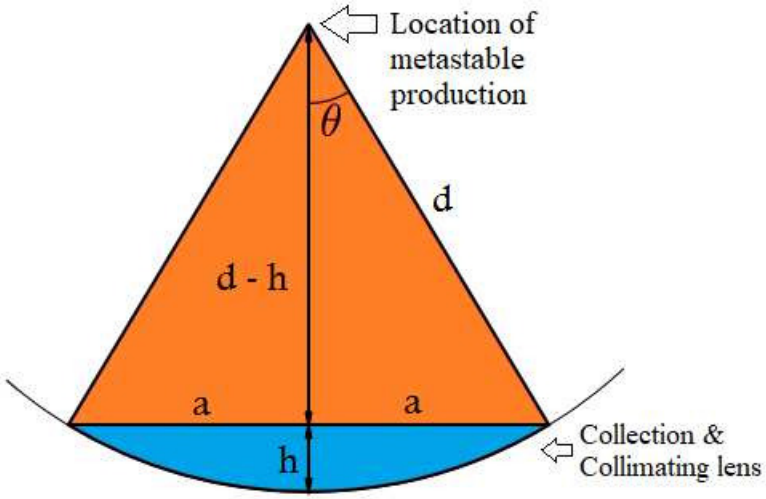

FIG. 37: Geometry of solid angle considerations.

$$\Omega = 2\pi(1 - cos\theta) \tag{34}$$

where

$$\theta = \sin^{-1}(\frac{a}{d}) = 6.075^{\circ} \tag{35}$$

and a is the radius of the collimating lens, d is the distance from the produced metastables to the rear of the lens.

$$\Omega = 0.035 \text{ steradians}$$

The surface area of the spherical edge of the collimating lens is

$$\frac{\Omega}{4\pi \text{ steradians}} = 0.027$$

Using the above calculations, we can find the number of counts we expect to see via the PMT per second:

counts per second = (photons per second)($\Omega/4\pi$str)(760nm min. filter transmission)(quantum efficiency of the PMT)(% due to discriminator level)

$$\frac{\#\text{counts}}{\text{s}} = (597,907\frac{\text{photons}}{\text{s}})(0.027)(50\%)(4\%)(0.26) = 83.95 \text{ counts/s}$$

In terms of pressure:

$$\frac{\#\text{counts}}{\text{s}} = (8.97 \times 10^8 p)(0.027)(50\%)(4\%)(0.26) = 1.26 \times 10^5 p \text{ counts/s}.$$

where p is pressure.

This is what we would expect with both the laser locked and the Fabry-Perot cavity locked. This is a signal we could see using our PMT. However, we need to also take into account the amount of noise we expect to see. Doing the experiment in the dark with both the RGA and the ion gauge off allowed us to reduce our dark counts to no more than 0-3 counts per 5s. The data for the detected krypton lamp photons from scattering in the chamber (at a fixed photon counter discriminator level to significantly reduce dark counts) is shown in Table 3. Note that the total counts will depend on the discriminator level. Characterization of the PMT detector to ascertain the best discriminator level to optimize signal noise will be conducted in the future. The PMT was operated at room temperature, but PMT dark counts can be nearly eliminated by cooling the PMT. Furthermore, lamp photon detection can be reduced by a more sophisticated optical collection line that uses apertures.

TABLE 3: Counts in 5s taken with only Krypton Lamp on.

Photon Counts	Settings	
350	Discriminator	50mV
350	Gain	0.8V
370	Time	5s
410		
370		
400		
430		
390		
400		
390		

To calculate our expected noise, using Table 3, our sample mean is:

$$\overline{x} \equiv \frac{1}{n}\sum_{k=1}^{n} x_k = 386 \text{ counts}$$

where $n = 10$ and x is the number of counts in 5s from the lamp light alone. Our sample variance is:

$$s^2 \equiv \frac{1}{n-1}\sum_{k=1}^{n}(x_k - \overline{x})^2 = 671$$

and the standard deviation is:

$$\sigma_x^2 = \frac{s^2}{n} = 67.1$$

$$\sigma_x = 8.2 \text{ counts}$$

For this set of parameters, we get a background of

$$\overline{x} \pm \sigma_x = 386 \pm 8.2 \text{ counts}$$

every 5 seconds, so we would expect 77.2 counts per second of noise. This indicates a signal to noise of $\frac{84}{77.2} \approx 1.09$ at a pressure of 5×10^{-6} Torr which is definitely a signal that could be seen by our PMT. In terms of pressure to get a signal to noise of 1, we would need

$$\frac{\#\text{counts}}{\text{s}} p = \frac{\text{noise counts}}{\text{s}}$$
$$1.26 \times 10^5 p = 77.2,$$

so

$$p = 6.13 \times 10^{-4} Pa = 4.6 \times 10^{-6} \text{ Torr}$$

Note that the current experiment can be done in an atomic beam or a cell. Alternative detection schemes, such as detection of resonant scattering of metastable krypton at 811nm are also possible. Because this transition is closed, light scattering will not quench the metastable state allowing for several photons (10-20) to be scattered by each metastable atom in the beam, limited by transit time through the

811nm light. Atoms can be quenched via collisions with background gas, however, so care must be taken to ensure that mean free path in the chamber is not less than the distance between metastable krypton creation and 811nm light scattering.

CHAPTER 5

CURRENT STATUS AND FUTURE PROSPECTS

5.1 CURRENT STATUS

At present, while the apparatus is built and ready to be optimized, there are still items to address before proper data collection for characterizing metastable krypton production can begin. We successfully locked the 819nm laser, and had planned to optimize the location of the PMT and then do a preliminary test to see if we saw any indication of metastables produced - even with the cavity not stabilized. However, right as we were getting ready to move on to the next step of optimizing the location of the PMT, the krypton vapor cell began to fail and the cell would go out unexpectedly and became more and more difficult to light. The failure was in a characteristic manner that has been observed in discharge cells before. This means we could no longer see saturated absorption, which was vital to the experiment.

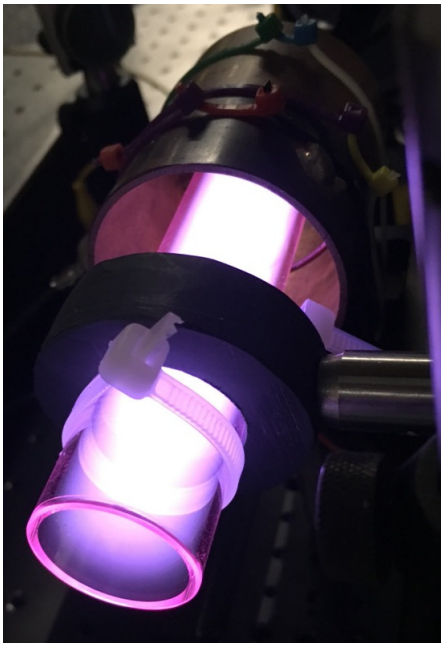

FIG. 38: Tell-tale red rim of dying krypton cell.

5.2 FUTURE PROSPECTS

While this means the end of this thesis, once a new krypton vapor cell is bought or built the production of metastable krypton via our methods should be successful. First and foremost, before detection, the PMT's location needs to be optimized and the optics train improved to reduce the detection of lamp photons.

Second the cavity needs to be stabilized or "locked." Locking the cavity will ensure that it is always on resonance and that the power build-up is maximized and constant. To improve the signal to noise, we can take a second look at the discriminator level, it may have been set too high. Also, there is a newer version of our 123.6nm lamp (with higher photon flux) that is now available that could be incorporated.

In addition, choosing a larger volume power build-up cavity with higher finesse would lead to more atoms excited. We were largely working with what was readily available in the lab for this first demonstration (proof of principle) of the all-optical excitation apparatus, but these improvements should find their way into the final design.

As mentioned earlier, we can also explore excitation to the $5p[5/2]_{J=3}$ state with 811nm light, which will allow the atoms to cycle and increase the number of photons detected / metastable atoms produced.

Finally, our eventual goal would be to add in differential pumping to our chamber to conclusively demonstrate that all-optical excitation without quenching the metastables at a metastable atom flux needed for implementation by ATTA is achievable.

BIBLIOGRAPHY

[1] Z.-T. Lu, "Radiokrypton dating coming of age," National Science Review **3**, 172–173 (2016).

[2] C. Buizert, D. Baggenstos, W. Jiang, R. Purtschert, V. V. Petrenko, Z.-T. Lu, P. Müller, T. Kuhl, J. Lee, J. P. Severinghaus, and E. J. Brook, "Radiometric 81kr dating identifies 120,000-year-old ice at taylor glacier, antarctica," Proceedings of the National Academy of Sciences **111**, 6876–6881 (2014).

[3] W. Jiang, G.-M. Yang, J.-Q. Gu, S.-M. Hu, and Z.-T. Lu, "Radiokrypton dating with atom trap trace analysis," Procedia Earth and Planetary Science **17**, 41–44 (2017).

[4] C. Y. Chen, Y. M. Li, K. Bailey, T. P. O'Connor, L. Young, and Z.-T. Lu, "Ultrasensitive isotope trace analyses with a magneto-optical trap," Science **286**, 1139–1141 (1999).

[5] M. Kohler, P. Sahling, C. Sieveke, and G. Kirchner, "All-optical atom trap trace analysis–potential use of 85kr in safeguards activities," Tech. rep., University of Hamburg (2015).

[6] W. Jiang, K. Bailey, Z.-T. Lu, P. Mueller, T. P. OConnor, C.-F. Cheng, S. M. Hu, R. Purtschert, N. C. Sturchio, Y. R. Sun, W. D. Williams, and G.-M. Yang, "An atom counter for measuring 81Kr and 85Kr in environmental samples," Geochimica et Cosmochimica Acta **91**, 1 – 6 (2012).

[7] L. Young, D. Yang, and R. W. Dunford, "Optical production of metastable krypton," Journal of Physics B: Atomic, Molecular and Optical Physics **35**, 2985–2992 (2002).

[8] M. Kohler, H. Daerr, P. Sahling, C. Sieveke, N. Jerschabek, M. Kalinowski, C. Becker, and K. Sengstock, "All-optical production and trapping of metastable noble-gas atoms down to the single-atom regime," EPL (Europhysics Letters) **108**, 13001 (2014).

[9] P. S. Light, M. A. Dakka, R. Glover, R. Sang, and A. N. Luiten, "Laser-based noble-gas metastable excitation techniques with application to atom trap trace

analysis," in "CLEO: Science and Innovations," (Optical Society of America, 2017), pp. SW4O–1.

[10] M. A. Dakka, G. Tsiminis, P. S. Light, R. D. Glover, C. Perrell, J. Moffatt, N. A. Spooner, R. T. Sang, and A. N. Luiten, "Laser-based metastable krypton generation," (2018).

[11] G. White, "Private communication," (2018).

[12] A. Kramida, Yu. Ralchenko, J. Reader, and and NIST ASD Team, "Nist atomic spectra database," (2017).

[13] W. T. Silfvast, *Laser Fundamentals* (Cambridge University Press, 2004), 2nd ed.

[14] C. J. Foot, *Atomic Physics* (Oxford University Press, 2005).

[15] R. Compton and M. Duncan, *Laser Experiments for Chemistry and Physics* (Oxford University Press, 2016).

[16] W. Demetroder, *Laser Spectroscopy 1- Basics* (Springer, 2011).

[17] R. Paschotta, *External-cavity diode lasers* (WILEY-VCH, 2008).

[18] Resonance Ltd., 143 Ferndale Drive North, Barrie Ontario, L4N 9V9, Canada, *RF Powered VUV Line Sources With Quick Disconnect and Extension Operations* (2012). Model : KrLM-LQD12.

[19] Stanford Research Systems, Inc., 1290 D Reamwood Avenue Sunnyvale, CA 94089, *Model Sr400 Gated Photon Counter* (1988).

VITA

Lindsay M. Thornton
Department of Physics
Old Dominion University
Norfolk, VA 23529

EDUCATION:

MS, Physics, Old Dominion University, Norfolk, VA, (expected 8/2018). Thesis title: "Fabrication of An Apparatus for All-Optical Production of Metastable Krypton."
BS (May 2016) Mathematics and Physics, East Carolina University, Greenville, NC.
BA (May 2003) Environmental Studies, Drama, and Biology, Washington College, Chestertown, MD.

GRADUATE ACADEMIC AWARDS:

Three Minute Thesis Competition Winner and People's Choice Winner, Old Dominion University, 2018.
Outstanding Teaching Assistant Award, Old Dominion University, 2017.

RESEARCH EXPERIENCE:

Undergraduate Research Fellow, National Institute of Standards and Technology (NIST), Gaithersburg, MD, Summer 2015.
Student Researcher, East Carolina University Physics Department, Greenville, NC, 2014 – 2016.

WORK EXPERIENCE:

Old Dominion University
Online Algebra-based Physics Lab Curriculum Developer, Spring 2018.
Teaching Assistant- Calculus-Based Physics Class, Spring 2018.
Laboratory Instructor- Introductory through Calculus-based Physics, 2016-2018.
East Carolina University and Pitt Community College
Teaching Assistant, Summer Ventures, Summer 2016.
Teaching Assistant, Remedial Math Class, 2013, and 2015 – 2016
Lead Physics Tutor and Summer Teaching Assistant, 2014 – 2015.
NC Aquarium at Pine Knoll Shores
Education Programs Specialist, 2006 – 2012

Typeset using LaTeX.